UNIVERSITY OF OKLAHOMA

GRADUATE COLLEGE

FRICTIONAL PROPERTIES OF FAULT GOUGE IN HIGH-VELOCITY/LONG-DISTANCE SHEAR EXPERIMENTS

A THESIS

SUBMITTED TO THE GRADUATE FACULTY

in partial fulfillment of the requirements for the

Degree of

MASTER OF SCIENCE

By

BARRETT CHANCE MORGAN
Norman, Oklahoma
2016

FRICTIONAL PROPERTIES OF FAULT GOUGE IN HIGH VELOCITY/LONG-DISTANCE SHEAR EXPERIMENTS

A THESIS APPROVED FOR THE
CONOCOPHILLIPS SCHOOL OF GEOLOGY AND GEOPHYSICS

BY

_____
Dr. Ze'ev Reches, Chair

_____
Dr. Andrew Elwood Madden

_____
Dr. Roger Slatt

Acknowledgements

I would like to thank my advisor and mentor Dr. Ze'ev Reches to whom I owe my gratitude for allowing to me to pursue my interest in scientific research. Dr. Reches was extremely patient throughout my entire master's research and helped me to achieve the research and personal goals I set for myself.

I would also like to thank the many colleagues that I have had to honor of getting to know on a professional and personal level throughout my time at the University of Oklahoma. Many hours were spent in and outside the lab discussing and supporting my work. Thanks to Simon Zu for his continuous help in the lab, Brett Carpenter for his extensive help not only in the lab, but also on the drill site in New Zealand, Jianjun Li for running many experiments for me, Wen Qi for her feedback during our research group meetings, Bill Doyle for his assistance in the lab, and Jefferson Chang for his feedback during our group meetings. I would like to thank Marco Scuderi at INGV for helping bridge data gaps for the research on the Alpine Fault and going out of his way to conduct several experiments.

I would also like to thank my wife, Karrie, and daughter, Maddox, for allowing me to pursue my educational goals and the sacrifices they have made that allowed me to finish my degrees. Without their support, this would have been achievable.

Financial support for this research was provided by NEHRP-USGS award G13AP00048 "Gouge Rheology During Earthquake Slip, Part II: Experimental Investigation", NSF-Geophysics award 1345087 "Experimental simulation of earthquake rupture processes", and by continuous support by ConocoPhillips and Anadarko Oil to my advisor, Dr. Ze'ev Reches

Table of Contents

List of Tables

List of Figures

Abstract

The present objective is the characterization of the dynamic friction and seismic stability of fault gouge in high-velocity/long-distance shear experiments. The study has two parts based on the gouge source: A) Reservoir rocks and mixtures of quartz-calcite-clay to determine the effect of gouge composition on frictional properties; and B) gouge of the Alpine Fault zone, New Zealand, which is a major plate boundary in the later stage of the seismic cycle. Accordingly, the abstract includes two parts.

DYNAMIC FRICTION AS FUNCTION OF FAULT-GOUGE COMPOSITION

The seismic stability of a fault and its likelihood to generate earthquakes are controlled by its frictional properties (Brace and Byerlee, 1966). This project focuses on experimental characterization of the frictional properties of rocks and sediments. The results will contribute to a better understanding of the seismicity associated with hydrocarbon production and wastewater injection, which are known to trigger seismic slip on faults and fractures (Segall, 1989, Ellsworth, 2013).

The experimental analysis is based on shearing rock gouge samples at slip-velocities up to 0.5 m/s, which is comparable to seismic slip velocity. The samples were placed in a confined rotary cell, and were sheared as either room-dry or water-saturated. Two types of samples were used: (1) core samples from six oil reservoirs comprised of approximately equal amounts of quartz and clay, and calcite that varies between 10% and 90%; and (2) mixtures of quartz-calcite-clay grains that cover a wide range of sedimentary rock compositions. The core samples were ground into aggregates of 150-450 μm before testing. The 93 experiments were conducted at slip velocities of 0.001-0.5 m/s with either stepped-velocity or constant velocity to distances up to 15 m.

The main results are: (1) the friction coefficient ranges widely from very low (~ 0.1) to very high (~1.2) with low strength of the water saturated samples, and weakening intensity proportional to the relative abundance of calcite in the samples; (2) The velocity-dependence of friction showed complex trends of velocity-weakening, velocity-strengthening, or velocity-neutral behavior.

DYNAMIC STRENGTH OF ALPINE FAULT GOUGE

The Alpine Fault, New Zealand, is a large plate boundary fault with slip rate of ~ 37 mm/y, and a documented history of M~8 seismic events (Sutherland, 2007). Trench analyses have shown that slip frequently ruptures to the surface, and suggest that a large earthquake occurs approximately every 300 years (Wells et al., 1999; Berryman, 2012). As the last known event occurred in 1717, the Alpine Fault is late in the seismic cycle (Sutherland, 2007).

To better understand the slip behavior and related hazards of the Alpine Fault, we analyze the frictional properties of its gouge that was collected at three field exposures (Waikukupa, Cataclasite, and Gaunt) along 40 km stretch of the Alpine Fault. The bulk samples (1-3 kg) were first manually disintegrated without shear, and then sieved to the 250-350 μm fractions. The gouge was sheared at natural, moisture-rich conditions at slip-velocity range of 0.01-1.5 m/s in stepped-velocity style with a constant normal stress of ~3 MPa. Data collection included monitoring the CO_2 and H_2O emission, in addition to the standard mechanical parameters.

The results show an initial friction coefficient of μ ~0.6. Initial slip at low velocities (0.01 m/s) displays gentle velocity strengthening that changed to a drastic weakening (~50%) at velocity of 0.5 m/s. This weakening was associated with intense slip

localization along a hard, dark slip surface within the gouge zone. After the establishment of this slip surface, there was no strength recovery and the sample remains weakened. If such behavior occurs during a natural earthquake, it will allow the release of a significant amount of the accumulated energy, which may result in a stronger earthquake with larger displacement.

Chapter 1: Introduction

BASICS OF EARTHQUAKE PROCESSES

Earthquake instability is driven by dynamic weakening of a fault zone when slip initiates at a nucleation site (Brace and Byerlee, 1966; Kanamori, 1994). The weakening reflects the drop of frictional strength from a high "static" value to a low "dynamic" value. For many rocks, this drop is related to slip-velocity (Dieterich, 1978), displacement (Kanamori, 1994), acceleration (Chang et al., 2012) and the fault conditions (e.g., healing, temperature)(Dieterich, 1978). A central observation is the strong dependency of frictional behavior on fault composition. For example, faults made of gabbro or carbonates systematically become weaker as slip-velocity increases (Shimammoto 2005, Boneh et al., 2014). On the other hand, faults made of granite or diorite first become weaker as velocity increases up to a critical level of 0.05-0.1 m/s, and then become stronger with increasing slip-velocity (Reches and Lockner, 2010; Liao and Reches, 2012).

In general, fault slip has two end members: the unstable, fast slip that is seismic with associated ground shaking, and stable, creeping slip that is aseismic without earthquakes. These two slip modes, **seismic vs. aseismic**, reflect the mechanical character of the fault-zone. Experimental and theoretical analyses have revealed that the seismic vs. aseismic character is controlled by fault composition (Chen at al., 2016) and environmental conditions like temperature, stress and fluids (Blanpied et al., 1995).

FAULT-GOUGE COMPOSITION AND INDUCED EARTHQUAKES

The present study may provide better understanding for the recent increase of seismic activity in the US mid-continent (Peterson et al., 2016) (Fig. 1, 2). This activity raised two central, interrelated questions:

A. Why injection in some regions induces many earthquakes, e.g., central-north Oklahoma, whereas injection in other regions, e.g., South Dakota or Texas, induces no or few events (Fig. 2);
B. What controls the tendency of a rock-unit or a fault-zone to be triggered by fluid injection and to produce earthquakes;

It is possible that fault-gouge composition controls the seismic vs. aseismic mode in the central US including Oklahoma. Surprisingly, the dependence of seismic stability on the composition of fault-gouge has not been systematically studied, in spite of their profound impact on seismicity. One application of the present experimental analysis is to base the likelihood of seismic stability on rock composition.

The mid-continent of North America has historically been a tectonically inactive area with low levels of seismic activity, excluding, for example, localized events like the New Madrid events of 1811-1812 (Ellsworth, 2013). Beginning in the 1970's, the recording of these seismic events has steadily increased, possibly due to the denser array of seismometers. Beginning in 2008, seismic activity increased drastically with majority of the events in central Oklahoma, and the activity propagated with time from the south to north (Ellsworth, 2013).

This surge of earthquakes in Oklahoma is attributed to prolonged wastewater injection as part of decades of hydrocarbon production (Ellsworth, 2013: Keranen et al.,

2014: Walsh and Zoback, 2015; McNamara, 2015; Peterson et al., 2016). Fluid injection has been known to induce earthquakes since the Denver earthquake sequences at the Rocky Mountain Arsenal in the 1960's (Healy et al., 1968). Fault slip occurs once the shear stress along the fault exceeds its frictional strength, leading to creep or a seismic event. The failure condition for slip is expressed by Coulomb relations including:

$$\tau_{crit} = \mu(\sigma_n - P) + \tau_o \qquad \text{Equation 1}$$

where the critical shear stress τ_{crit} equals the product of the coefficient of friction μ and the effective normal stress given by the difference between the applied normal stress σ_n and the pore pressure P; τ_o is the fault cohesion (Jaeger and Cook, 1969). Thus, a fault may slip due to increase of shear stress, reduction of normal stress, or increase of pore pressure. It is commonly assumed that water injection into the subsurface can induce fault slip by two mechanisms; direct injection into a fault zone and raising its pore-pressure, or changing the stress field in the crust that may increase the shear stress or reduce the normal stress on remote faults (Fig. 1).

A central assumption of the present study is that while water injection may induce slip along faults, the mode of slip, namely seismic or aseismic, is primarily controlled by the faults composition. For example, the presence of talc was proposed as controlling the creep along the San Andreas Fault (Moore and Rymer, 2007). Thus, the present experimental work explores the control of gouge stability by its composition.

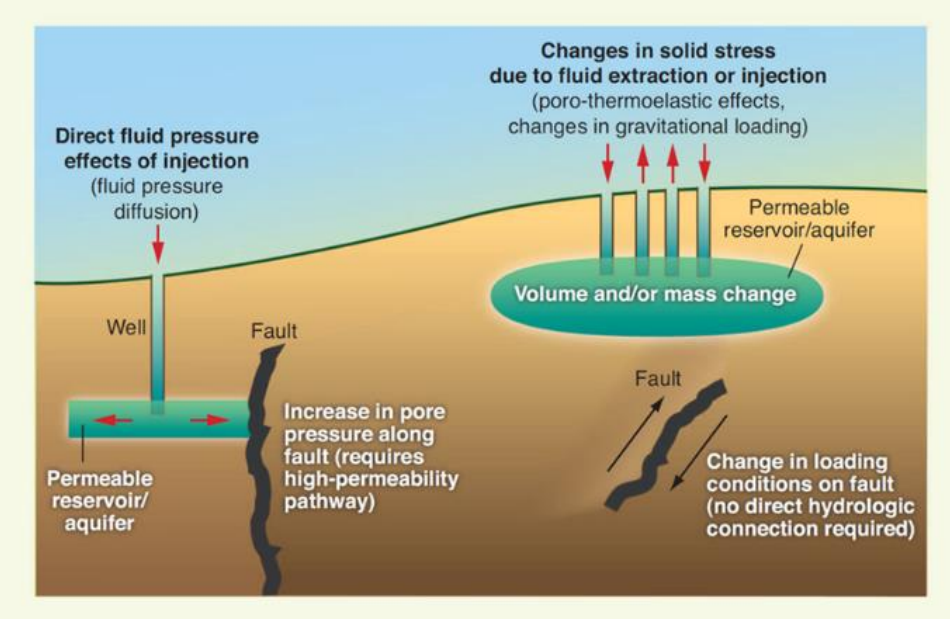

Figure 1. Mechanisms of inducing fault slip involve increase of pore pressure or a change in the stress field (Ellsworth, 2013).

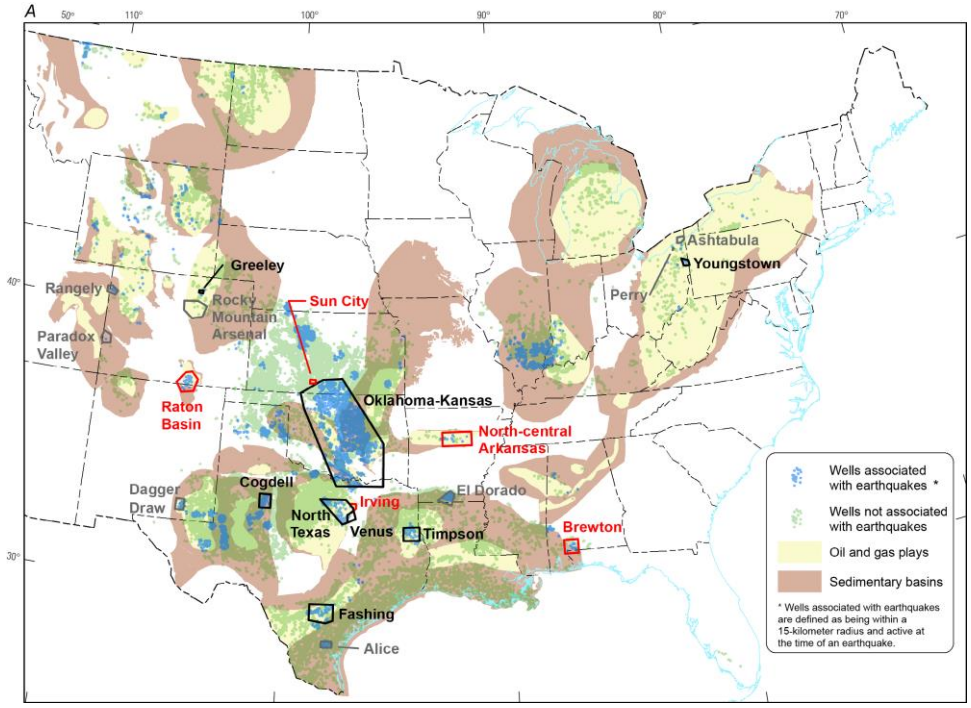

Figure 2. Map of the central US highlighting the wells associated with earthquakes and also the wells not associated with seismic events overlain by the regional oil and gas plays in their respective sedimentary basins (Peterson, 2016).

THE ALPINE FAULT

The Alpine fault is a large plate boundary between the Pacific and Australian plates, and which is exposed on the south island of New Zealand (Barnes et al., 2005; Sutherland et al., 2007). This fault accommodates the plate motion by right-lateral, transpressional slip. The on-shore, exposed part of the fault is about 800 km long (Fig. 3), and it is composed by right-stepping segments, small pull-apart basins, and ridges (Barnes et al., 2005; Sutherland et al., 2007). The gaps between the stepping segments are smaller than 5 km, and the rupture of a large earthquake can easily jump across such small gaps and continue along the trace of the fault (Norris et. al., 1990, Harris and Day, 1999). Assuming similar fault structure at depths (Berryman, 2012), large earthquakes of M ~ 8 are expected to occur along the Alpine Fault.

The strike-slip component of slip along the Alpine fault was evaluated as 27±5 mm/y, and it caused rapid exhumation of 6-9 mm/y of the crust from 20-30 km depths (Norris and Cooper, 2001, Little et al., 2002). Namely, the strike-slip component is ~ 75% of the fault-parallel motion with ~ 25% of dip-slip. Since about 1800, there has not been a large earthquake with surface rupture on the Alpine Fault. Paleoseismic analyses of the fault, including radiocarbon dating of forest damage and landslides, restrict the three recent events in the central region of the South Island to 1717, 1620, and 1430 (Sutherland et al., 2007). Trenches across the Alpine Fault near Haast and Okuru show extensive seismites including liquefaction, sand dikes, and sand extrusions, which are consistent with shaking of intensity of M>7. These results imply that the Alpine Fault ruptures every 300-400 y in large earthquakes, this implies that it moves episodically in large earthquakes as high as Mw~8.0 (Sutherland, 2007), and that it is currently late in its seismic cycle (Berryman, 2012).

For the above features of the Alpine fault, it is considered a prime candidate for scientific drilling with the main objective of monitoring the preparation for a major earthquake (Townend et al., 2009). The first phase of the Deep Fault Drilling project (DFDP) into the Alpine fault, 2011, resulted in two boreholes that penetrated the primary slip zone at depths of 96 m and 151 m (Boulton, 2014). The second phase of the drilling program (DFDP-2) of 2014 had a ~900 m deep borehole that did not reach the primary slip zone. Instrumentation for continuous monitoring of temperature, pressure, and seismic activity has been installed at ~400 m depth. The potential of extremely large earthquake along the Alpine fault pose major hazard to the South Island population.

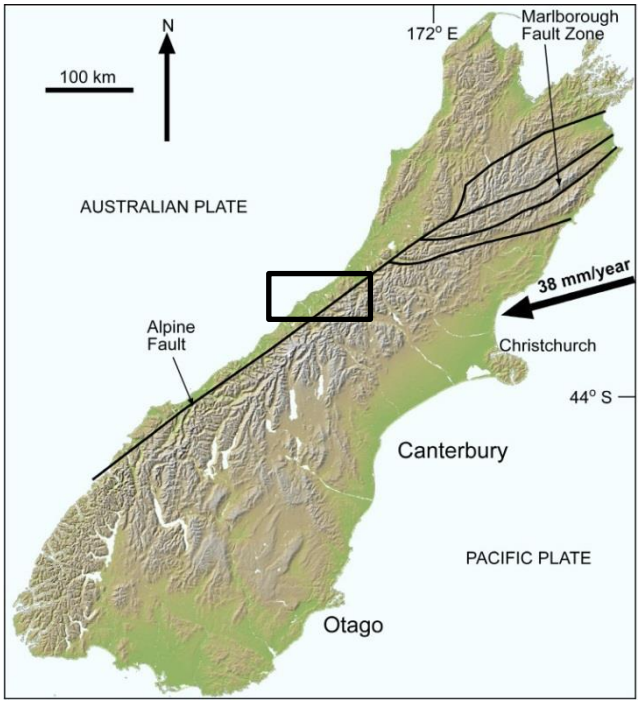

Figure 3. Map of the Alpine fault on the South Island, New Zealand and note the area of focus for this research indicated by black rectangle (www.otago.ac.nz)

PRESENT THESIS

Objectives

The present objective is the characterization of the dynamic friction and seismic stability of fault gouge in high-velocity/long-distance shear experiments. The study has two parts based on the gouge source and potential applications.

The first part examines the properties of reservoir rocks and mixtures of quartz-calcite-clay to determine the effect of gouge composition on frictional properties. It is envisioned that developing a stability database for these gouge compositions will help to delineate potential seismic hazards in the US mid-continent where induced seismicity by wastewater injection in on the rise (Fig. 1, 2).

The second part examines the frictional properties of gouge from the Alpine Fault zone, New Zealand, which is a major plate boundary in the later stage of the seismic cycle (Fig. 3). The present analysis will contribute to better understanding the rupture characteristics of this fault, e.g., co-seismic slip, weakening and healing.

Organization

Chapter 1 Introduction (this chapter)

This chapter is an introduction to the two focuses of the research with short introductions to basic rock mechanics dealing with seismic slip and an introduction to the geologic setting of the Alpine fault.

Chapter 2 Experimental methodology

This chapter outlines the experimental set-up including loading system, control and monitoring systems, samples, and the limitations of the machine.

Chapter 3 Dependence of fault dynamic stability on gouge composition

This chapter outlines the experiments that focused on the reservoir rock and sedimentary mixtures. The loading styles, experimental results, result synthesis, discussion and conclusion of these experiments are presented in detail here.

Chapter 4 Dynamic Strength of Alpine Fault gouge

This chapter outlines the experiments that focused on the Alpine Fault gouge collected from the field. The loading styles, experimental results, synthesized results, discussion and conclusion are presented in detail here.

Chapter 2: Experimental Methodology

EXPERIMENTAL SET-UP

Apparatus

The present experiments were conducted in the earthquake experimental laboratory, University of Oklahoma (Reches and Lockner, 2010, Boneh, 2013). The laboratory has two main components: (1) The loading apparatus (Fig. 4), called Rotary Gouge Apparatus (ROGA); and (2) The confined shearing cell (Fig. 5), called Confined ROtary Cell (CROC).

The ROGA shear apparatus has the capability to apply normal stress up to 35 MPa, slip velocity of 0.001 to 2 m/s, rise-time to full velocity <0.1 s, and unlimited slip distance. It allows for continuous control on slip velocity, and high frequency, up to 10 kHz, continuous monitoring of experimental data including normal load, shear load, slip velocity, displacement, temperature, and dilation.

CROC is cell for shearing granular materials at confined conditions. It has a ring-shaped gouge chamber with inner and outer diameters of 63.15 and 82.70 mm, respectively, and gouge layer thickness up to 3 mm (Fig. 5). The top and bottom of the gouge chamber are grooved with radial, triangular teeth, 0.4 mm deep, that transfer the applied shear into the gouge (Fig. 5). The gouge chamber is sealed by two-pairs of graphite-Teflon seals, and each pair is internally pressurized to ~ 3 MPa to maintain the sealing (Fig. 5A). The present experiments were run under constant-velocity or velocity-stepping conditions and at constant normal stress.

Experimental Procedure

Assembling CROC for a typical experiment has the following steps (see Fig. 5 for parts, shape, and position):

1. The axial loading cylinder is assembled, including emplacement of the two pairs of seals.
2. The powder chamber is assembled and weighed.
3. The crushed and sieved gouge powder is poured into the powder chamber, and then compressed manually with a tool that fits into the powder chamber. Depending on composition and grain size the sample weight varied between 11 g and 15 g.
4. The sample chamber is placed in the lower base of CROC, and then the axial loading cylinder is matched into the lower base and powder chamber.
5. The pressure monitoring valves and vacuum connection are attached to the exterior, upper part of CROC.
6. The circular base for holding the eddy sensors (Fig. 5B) is connected to the CROC.
7. The fully assembled CROC is placed in ROGA, and the pressure pipes connections and thermocouple plug are connected to the ROGA system.
8. The final step is placing rubber disk between the axial cylinder and ROGA base for stability purposes.
9. Application of the normal stress.
10. Application of the seal pressure
11. After each experiment, the output was checked for pressure leak from the pressurized seals into the gouge chamber. The chamber pressure is monitored continuously, and we selected a practical limit as leak indicator: Pressure increase above 15% was considered as indicator of nitrogen leak into the

chamber. In such case, we used only the data before the leak. Leaks were detected in 30 out of 93 experiments, and their results are excluded from the analysis.

Loading styles:

1. Constant slip-velocity experiments that reveal the steady-state friction, the critical weakening distance, D_c, volumetric changes in the gouge, and the dependence of the friction parameters on the normal stress, slip-velocity and slip-distance.
2. Stepped velocity during which the applied slip-velocity was stepped from low to high and repeated. This procedure can reveal the dynamic frictional stability of the tested gouge as function of slip-velocity, and it may show the friction evolution under complex velocity history.
3. Water injection tests to explore the effect of increased pore pressure. Water was injected into the slipping gouge at either constant flow-rate or constant pressure

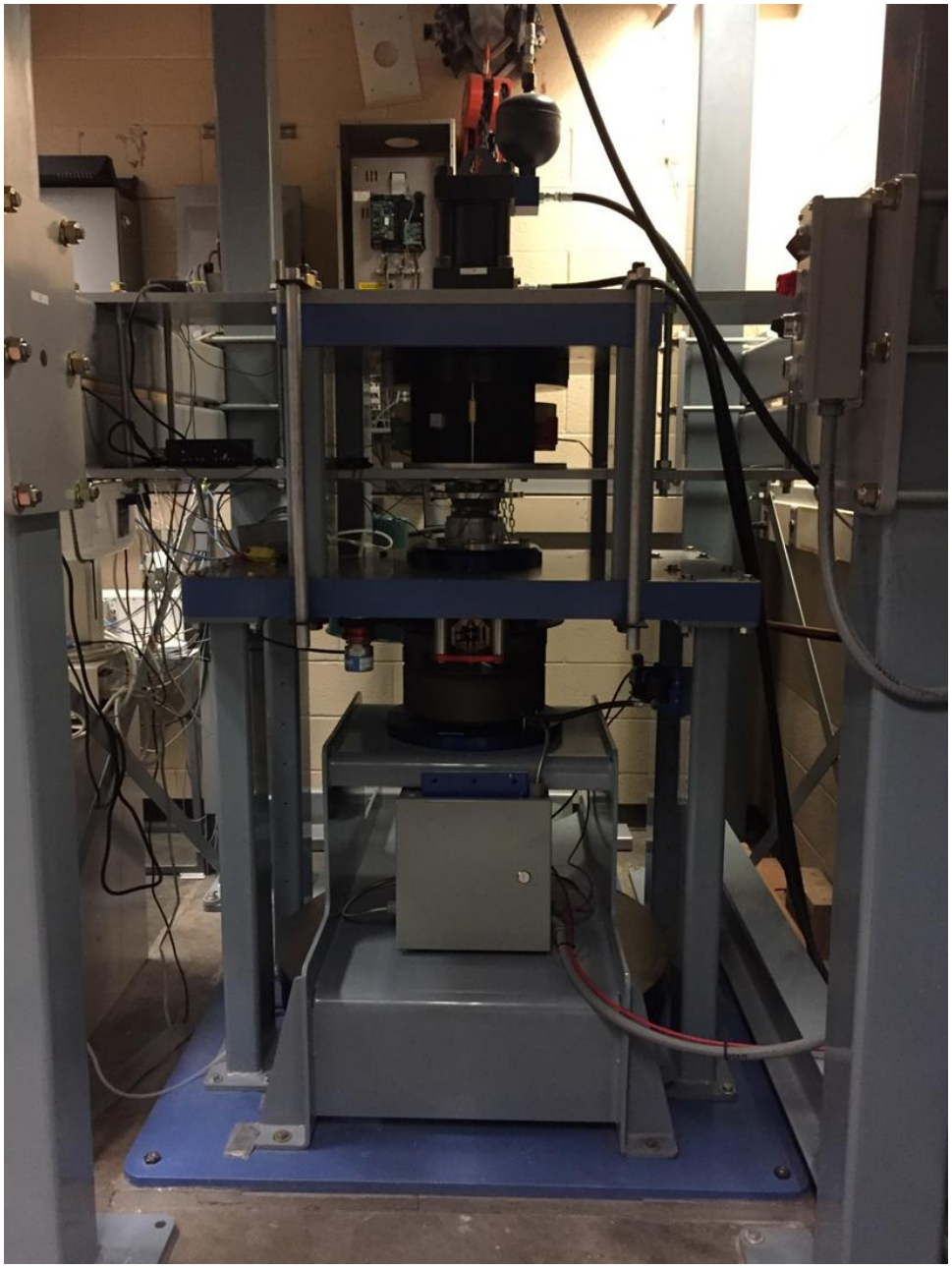

Figure 4. The ROGA apparatus in the earthquake simulation laboratory of OU.

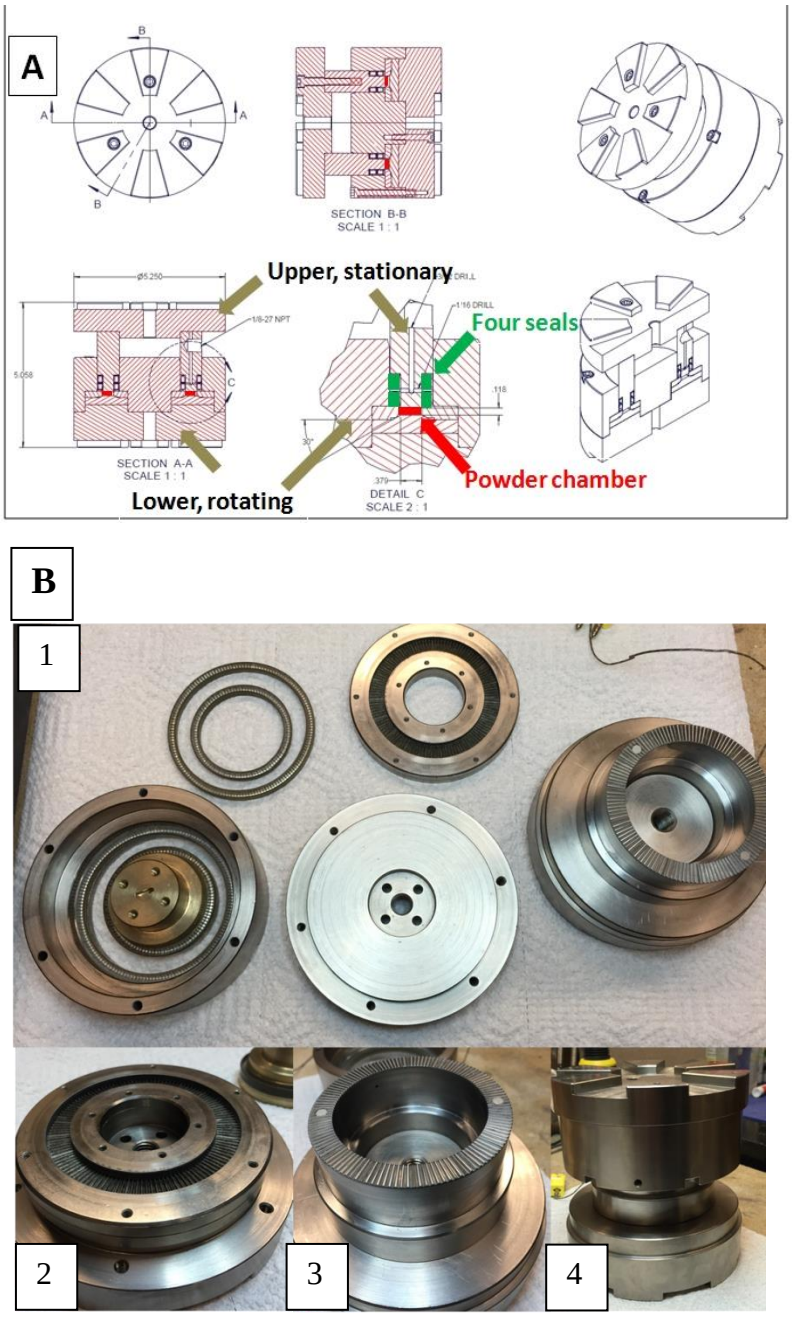

Figure 5. Top: (A) Draft of CROC, green arrows indicate location of ring-seals, red arrow indicate location of powder chamber, brown arrows indicate the upper and lower portions of CROC (B) Lower photos: (1) disassembled portions of the confined rotary cell; (2) lower, stationary, portion of CROC with sample chamber; (3) upper, rotating portion of CROC; (4) fully assembled CROC.

Chapter 3: Dependence of fault dynamic stability on gouge composition

Approach

A fault remains locked as long as the shear stress is lower than its frictional strength (equation 1). However, this equation does not predict if the fault slip will be stable (creep) or unstable (earthquake) once the shear stress exceeds the strength. The slip stability reflects the fault response: dynamic-strengthening leads to creep, whereas dynamic-weakening leads to earthquakes. I experimentally investigate the effect of fault composition on the stability mode.

The ultimate goal is to develop a database for the seismic stability that is based on the composition of sedimentary rocks. At this stage, I have analyzed the frictional behavior of six reservoir rocks and twelve compositional mixtures of quartz-calcite-clay (QCC). It is anticipated that the experimental results will serve as a tool to evaluate the likelihood of induced events for a given rock unit. I also examined the mechanisms of fault weakening (e.g., loading styles, saturation state of the gouge material, thermal pressurization powder lubrication, and grain rolling).

Sample Sources and Preparation

Reservoir Rocks

The samples used in this study were collected from several reservoirs in the continental US. The names and stratigraphic positions are unpublishable, and I use arbitrary names based on their quartz, calcite and clay composition (Table 1, Fig. 6). The core samples were fragmented and sieved to sand-size aggregates of 150-420 μm for the shear experiments. This grain-size was selected for ease of handling, and

apparently, even though it was not tested systematically, the initial grain-size has only small effect on the experimental friction (Xiaofeng Chen, personal comm. 2015).

Quartz-Calcite-Clay mixtures

I tested controlled mixtures of quartz-calcite-clay (QCC) as the first step to generate a database for the entire ternary diagram (Fig.6). The end-member components for the QCC mixtures includes pure quartz sand (>150 μm) supplied by US Silica, calcite (99% pure CaCO3) supplied by Alfa Aesar, and Montana montmorillonite powder supplied from R.K. Laros company. The QCC fault gouges were mixed proportionally by mass. The quartz was separated into coarse (150 μm) and fine (powder), and the other two components were used with the original clay grain size. The name of each mixture reflects its composition, e.g., QZ40-CC50-CL10 is a mixture of 40% quartz, 50% calcite, and 10% clay.

Table 1. Mineralogical composition of the tested reservoir rocks and Woodford Shale Samples (XRD)

	Quartz %	Calcite %	Clay %
RS-QZ22-CC53-CL25	22	53	25
RS-QZ07-CC90-CL03	7	90	3
RS-QZ40-CC00-CL59	40	0	59
RS-QZ32-CC62-CL06	32	62	6
RS-QZ32-CC17-CL51	32	17	51
RS-QZ09-CC83-CL08	9	83	8
WF-QZ67-CC1-CL32	67	1	32
WF-QZ77-CC00-CL23	77	0	23
WF-QZ68-CC02-CL30	68	2	30
WF-QZ79-CC00-CL21	79	0	21
WF-QZ69-CC00-CL31	69	0	31
WF-QZ68-CL00-CL32	68	0	32
WF-QZ57-CC10-CL34	57	10	34
WF-QZ64-CC10-CL27	64	10	27
WF-QZ59-CC04-CL37	59	4	37
WF-QZ63-CC10-CL28	63	10	28

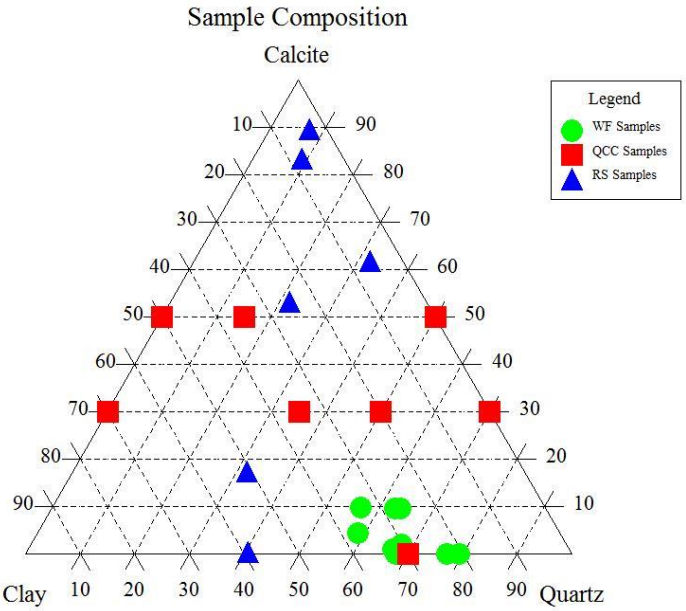

Figure 6. Ternary composition diagram of the tested samples (see text)

EXPERIMENTAL RESULTS

General Description

We conducted 93 experiments, including 67 on the reservoir rock samples and 26 on the QCC gouge samples, following the procedures described above. The tested samples had 14 different mineralogical compositions (Table 3, Fig. 6). The slip-velocity ranged 0.01 - 0.5 m/s, slip-displacements up to 15 m, and the normal stress was relatively constant at ~ 3 MPa. Most samples were tested room-dry, and four experiments were saturated with 20% wt distilled water; two of these tests included pressurized water injection during slip.

Loading Styles

Five typical experimental results are shown in Fig. 7, and the friction-velocity plots of all experiments are displayed in Appendix I. The constant velocity experiments on a room-dry sample (Fig. 7A) displayed relatively high friction, with (Fig. 7C) or without (Fig. 7A) slip-weakening. These experiments focused on the dynamic change of the frictional strength with slip-velocity and slip-distance. The stepped velocity experiments

(Fig. 7B, E) included multiple cycles of three alternating velocities, and constant slip-distance in each step. This loading style can reveal the evolution of the strengthening and weakening at velocity jumps. The water-saturated experiment (Fig. 7C) displayed a moderate friction coefficient with early slip-weakening followed by slip-strengthening. Finally, runs with water injection (Fig. 7D), displayed a distinct friction drop upon the injection.

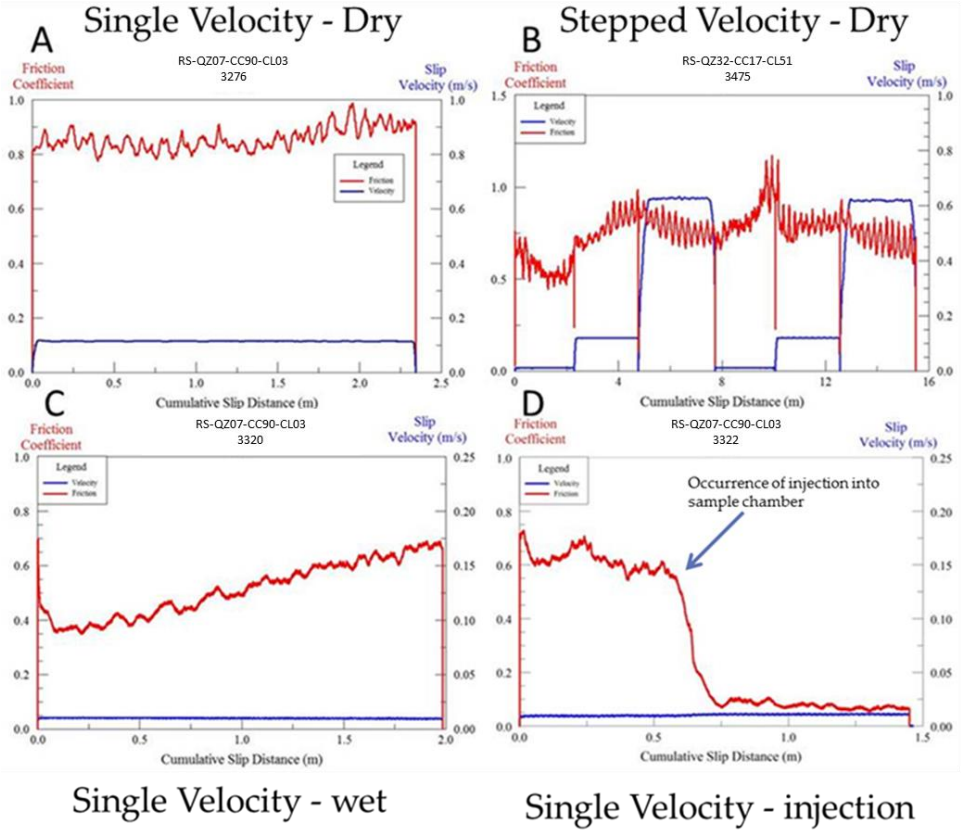

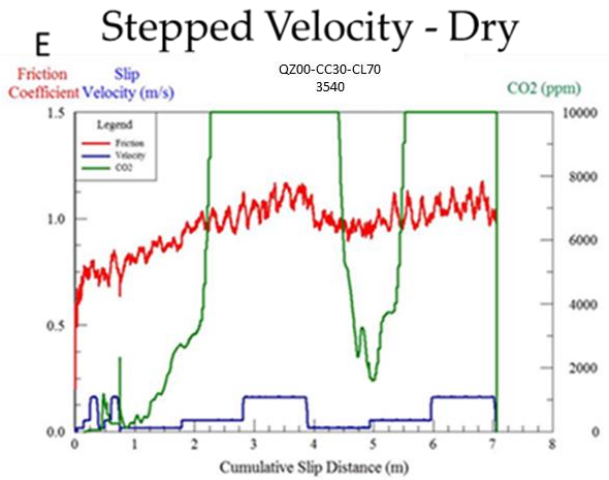

Figure 7. Friction coefficient (red), slip-velocity (blue) in reservoir rock experiments; sample name and run number shown on top of each plot; note different scales. (A) single velocity with room-dry gouge, (B) stepped-velocity experiment with the room-dry gouge, (C) single velocity experiment with saturated (20% wt) sample, (D) single velocity run with saturated (20% wt) sample, with pressurized water injection after 0.5 m of slip, (E) stepped velocity QCC with QZ=00%, CC=30%, and CL=70%, loaded by stepping velocity with CO_2 (green) monitoring; note that CO_2 curve is flat at 10,000 ppm due to limited CO_2 range setting.

Table 2. Reservoir rock experiments completed without significant leak.

Sample	Experiement #	Velocity - single/stepped (m/s)	σ_n (mpa)	dry/saturated	Cumulative Displacement (m)	Friction Coefficient
RS-QZ22-CC53-CL25	3270	0.01	2.8	dry	2.4	0.80
RS-QZ22-CC53-CL25	3270A	0.01	2.8	dry	0.5	0.93
RS-QZ22-CC53-CL25	3271	0.01	2.9	dry	2.4	0.74
RS-QZ22-CC53-CL25	3274	0.12	3	dry	2.5	0.33
RS-QZ22-CC53-CL25	3552	0.01-0.64	1.8	dry	12.5	NA
RS-QZ07-CC90-CL03	3275	0.01	2.8	dry	1.4	0.83
RS-QZ07-CC90-CL03	3276	0.12	2.8	dry	2.3	0.85
RS-QZ07-CC90-CL03	3277	0.01	2.8	dry	1.2	0.94
RS-QZ07-CC90-CL03	3278	0.11	2.8	dry	2.3	1.12
RS-QZ07-CC90-CL03	3280	0.01	2.9	dry	1.8	0.40
RS-QZ07-CC90-CL03	3281	0.01	2.9	dry	1.4	0.79
RS-QZ07-CC90-CL03	3282	0.11	2.8	dry	2.3	0.95
RS-QZ07-CC90-CL03	3283	0.01	2.8	dry	1.2	0.95
RS-QZ07-CC90-CL03	3284	0.11	2.8	dry	2.3	1.12
RS-QZ07-CC90-CL03	3286	0.01	2.9	dry	2.0	0.23
RS-QZ40-CC00-CL59	3287	0.01	2.9	dry	1.7	0.56
RS-QZ40-CC00-CL59	3288	0.12	2.8	dry	2.4	0.79
RS-QZ40-CC00-CL59	3290	0.12	2.8	dry	2.4	0.74
RS-QZ40-CC00-CL59	3291	0.60	2.8	dry	3.0	0.65
RS-QZ40-CC00-CL59	3351	0.01-0.63	1.8	dry	12.3	NA
RS-QZ40-CC00-CL59	3322	0.001	2.8	wet/injection	1.4	NA
RS-QZ32-CC62-CL06	3300	0.05	2.9	dry	2.4	0.57
RS-QZ32-CC62-CL06	3301	0.60	2.8	dry	3.0	0.49
RS-QZ32-CC62-CL06	3302	0.01	2.9	dry	1.5	0.62
RS-QZ32-CC62-CL06	3550	0.01-0.63	1.8	dry	6.9	NA
RS-QZ32-CC17-CL51	3303	0.01	3	dry	1.5	0.82
RS-QZ32-CC17-CL51	3304	0.12	2.8	dry	2.4	0.92
RS-QZ32-CC17-CL51	3305	0.01	3	dry	1.3	0.99
RS-QZ32-CC17-CL51	3306	0.11	3.1	dry	2.3	1.02
RS-QZ32-CC17-CL51	3307	0.60	3	dry	6.6	0.71
RS-QZ32-CC17-CL51	3308	0.01	3	dry	1.4	0.88
RS-QZ32-CC17-CL51	3475	0.01-0.55	2.1	dry	14.3	0.74
RS-QZ09-CC83-CL08	3314	0.01	3	dry	1.5	1.69
RS-QZ09-CC83-CL08	3323	0.01	3.1	wet	1.8	0.32
RS-QZ09-CC83-CL08	3324	0.11	3	wet	2.4	0.27
RS-QZ09-CC83-CL08	3325	0.01	3	wet	1.9	0.25
RS-QZ09-CC83-CL08	3326	0.11	3	wet/injection	2.4	NA
RS-QZ09-CC83-CL08	3327	0.6	3	wet	3	0.26
RS-QZ09-CC83-CL08	3328	0.01	3	wet/injection	2.1	NA

Table 3. Conditions and main results of QCC experiments.

Sample	Experiment	Velocity - single/stepped (m/s)	σ_n (mpa)	dry/saturated	Cumulative Displacment (m)	Friction Coefficient
QZ00-CC30-CL70	3540	0.020-0.170	2	dry	7	NA
QZ30-CC70-CL00	3541	0.020-0.170	2	dry	0.12	NA
QZ00-CC30-CL70	3543	0.020-0.170	2	dry	7	NA
QZ30-CC35-CL35	3544	0.020-0.170	2	dry	6.6	NA
QZ30-CC35-CL35	3545	0.020-0.170	2	dry	6.6	NA
QZ30-CC50-CL20	3546	0.020-0.170	2	dry	6.7	NA
QZ00-CC30-CL70	3547	0.020-0.170	2	dry	7	NA
QZ00-CC30-CL70	3548	0.162-0.325	2	dry	10	NA
QZ30-CC20-CL50	3549	0.325	2	dry	11	0.52
QZ30-CC20-CL50	3550	0.325	2	dry	11	0.5
QZ30-CC50-CL20	3551	0.325	2	dry	11	0.28
QZ30-CC50-CL20	3552	0.325	2	dry	6.6	0.64
QZ30-CC50-CL20	3553	0.325	2	dry	6.7	0.96
QZ30-CC50-CL20	3554	0.325	2	dry	6.7	NA
QZ50-CC50-CL00	3555	0.020-0.170	1.6	dry	7.1	NA
QZ50-CC50-CL00	3556	0.325	1.6	dry	10	0.31
QZ50-CC50-CL00	3557	0.325	2.2	dry	5.1	0.48
QZ50-CC50-CL00	3558	0.020-0.170	2.2	dry	7	NA
QZ50-CC00-CL50	3559	0.020-0.170	2.1	dry	7	NA
QZ50-CC00-CL50	3560	0.325	2.1	dry	10	0.92
QZ50-CC15-CL35	3561	0.020-0.170	2	dry	7	NA
QZ50-CC15-CL35	3562	0.050-1.000	2	dry	18	NA
QZ50-CC15-CL35	3563	0.012	2	wet	2	0.12
QZ50-CC50-CL00	3564	0.012	2	wet	1.1	NA
QZ50-CC50-CL00	3565	0.012	2	wet	1.1	0.5

SYNTHESIS OF EXPERIMENTAL RESULTS

The reservoir rocks and QCC samples have shown complex trends of slip velocity, slip-distance, and composition. The trends are presented on friction maps (Figs. 8, 9) in which the friction coefficients are shown in slip-velocity/slip-distance space, and the friction coefficient magnitude is displayed by the size of the symbol (Boneh et al., 2013; Chen et al., in prep.). It is necessary to use friction maps as the friction and fault stability may depend on both slip-velocity and slip-distance.

The friction maps of the reservoir rocks and QCC mixtures (Figs. 8, 9) reveal the following trends that are marked by black arrows (note scale of friction coefficient):

1. The friction coefficient for the gouge ranges widely from ~0.1 for saturated gouge (Fig. 7D) to < 1.0 (Fig. 9) for dry gouge.
2. The friction coefficient stays high, □ > 1.0, almost independently of velocity and displacement for gouge samples with high quartz content and no clay (QZ50-CC50-CL00 in Fig. 9A).
3. Samples of relatively high clay content display clear trends of slip-strengthening with gentle velocity-strengthening, e.g., RS-QZ40-CC00-CL59 in Fig. 8B and QZ00-CC30-CL70 in Fig. 9B.
4. Samples with relatively high calcite content show indications of slip-weakening, e.g., RS-QZ07-CC90-CL03 in Fig. 8A and RS-QZ32-CC62-CL06 in Fig. 8C.
5. A sample with equal amount of quartz and calcite (QZ50-CC50-CL00 in Fig. 9A) indicate relatively high friction with no clear trend of dynamic friction.
6. Pressurized injection of water during slip (Fig. 7D) leads to strength drop, as expected for the reduction of the effective normal stress.

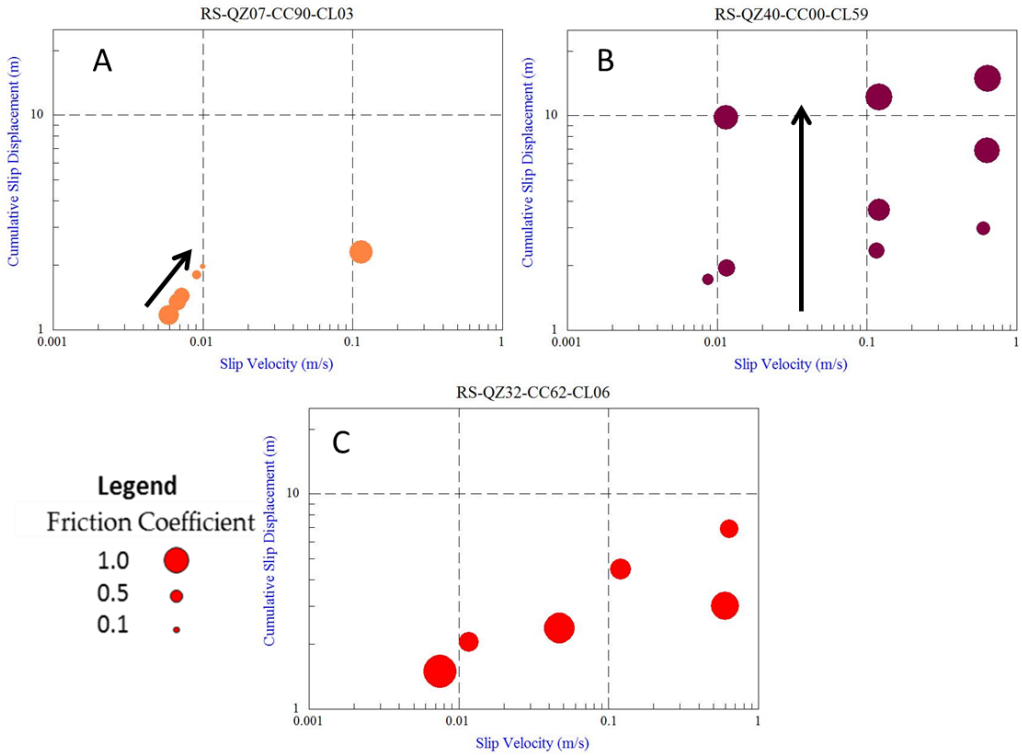

Figure 8. Friction maps for three reservoir samples that display friction coefficient as function of both slip velocity and slip distance. (A) RS-QZ07-CC90-CL03 under two separate loading conditions. The left group of dots in a single experiment under stepping velocities, which results in velocity-weakening and slight slip-weakening indicated by black arrow. The far right data point is a single velocity experiment which maintains the original strength of the material.(B) RS-QZ40-CC00-CL59 data showing a slip strengthening trend indicated by black arrow. As the slip distance is increased the friction increases. (C) RS-QZ32-CC62-CL06 no clear trend with current data points.

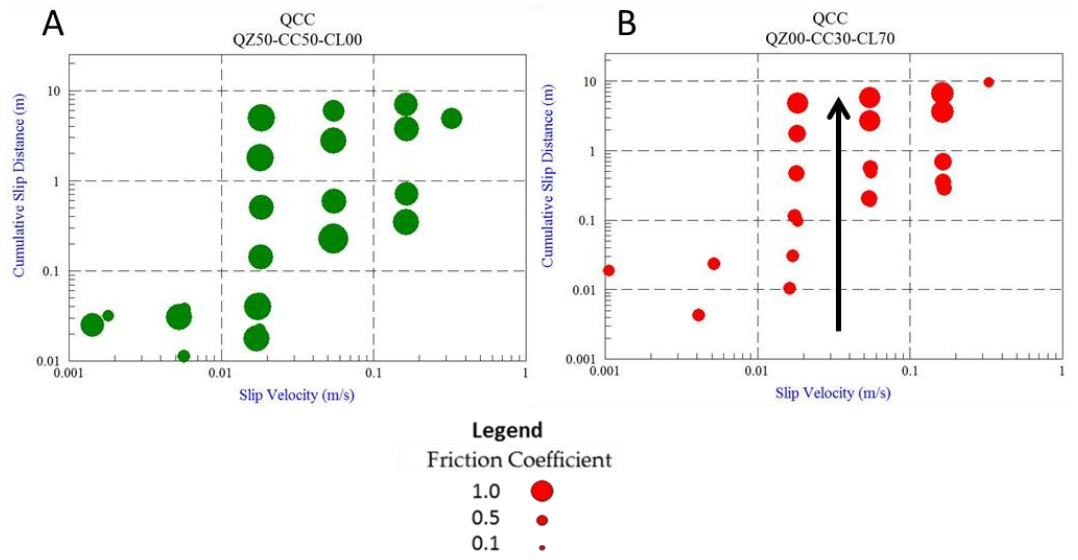

Figure 9. Friction maps for QZ50-CC50-CL00 and QZ00-CC30-CL70. (A)) No clear trend for velocity, slip, -strengthening, or –weakening (B) Trends of slip – strengthening.

MICROSCOPIC OBSERVATIONS

We epoxied seven samples of the sheared gouge zones and prepared five samples for microscopic and SEM analysis. We noted two modes of the shear distribution:

1. Slip localization along principal-slip-surface generated a shiny, locally smooth zone with slickenside striations down to scale of 100 microns (Fig. 11A). Even though the principal-slip-surface reflects light (Fig.11, B), which suggests that it is smooth (Siman - Tov et al., 2013), a close-up view (Fig. 11B) reveals local roughness (Chen et al., 2013). This roughness is also observed at SEM scale.

2. Distributed shear along the shear zone (cross-section in Fig. 11D) that appear as sets of Riedel shears and P shears (Chen et al., 2016).

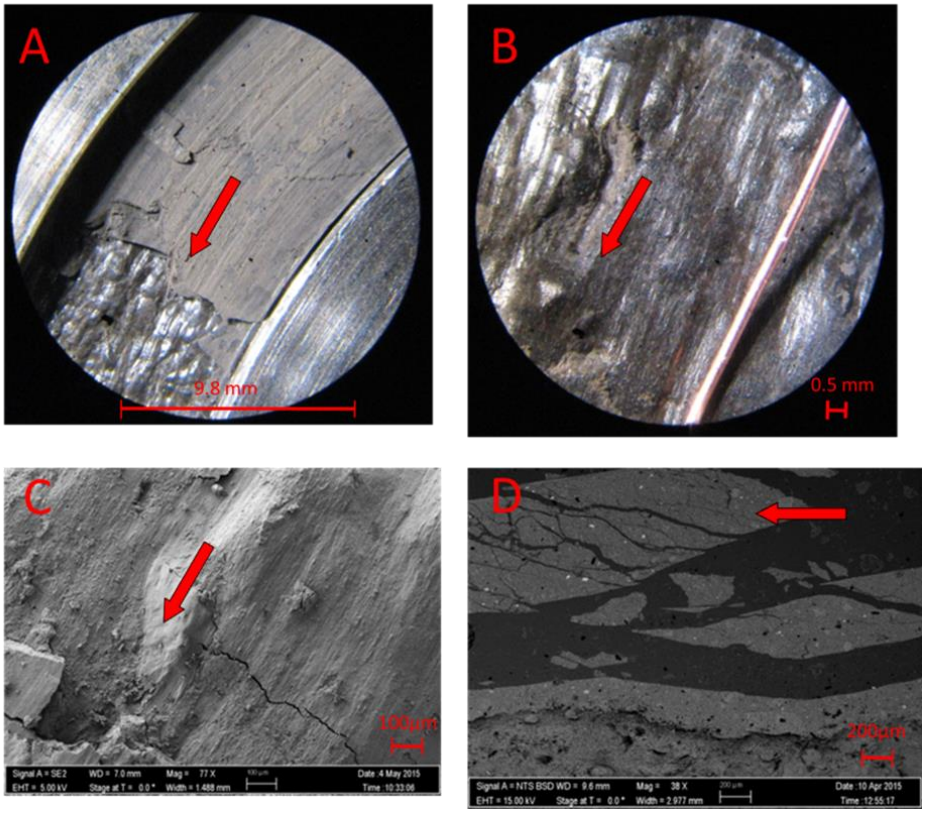

Figure 10. Microscopic photos taken at gradually smaller scales of RS-QZ32–CC17-CL51 (red arrow indicating direction of slip). (A) relatively smooth shiny localized slip surface occurred within gouge layer,(B) closer view of the localized surface with visible slickenlines, (C) SEM photo of localized surface with visible slickenlines and rougher surface, (D) SEM-electron backscatter photo of cross-section of slip-surface showing distributed shear (Riedel shear, P shear, and Y shear).

Chapter 4: Dynamic strength of Alpine Fault gouge

Approach

The present objective is to determine the frictional properties of this gouge at seismic velocities with emphasis on its potential weakening. These experiments will complement the previous, low velocity analysis by Boulton et al. (2012) who sheared the Alpine Fault gouge at slip-velocity range of 1 - 300 μm/s and normal stress of σn = 35 MPa. The results are anticipated to help in understanding the seismic potential of the Alpine fault.

Sampling

I participated in the DFDP-2 drilling project into the Alpine fault, November 2014. As part of the work, I collected gouge samples from three sites spanning ~40 km along the Alpine Fault trace (Fig. 11). Two of the sites are located on the active trace (Gaunt Creek, and Cataclasite Creek), and one site is on an abandoned trace of the Alpine Fault system (Waikukupa Creek). The samples were oriented in the field, and wrapped in plastic cover to preserve the natural state of the gouge.

The Gaunt creek sample was collected from an exposure (Fig. 12) of the fault trace near the first drilling site, DSDP. The gouge layer was 10-20 mm thick and incohesive. The XRD composition of this sample is 26% illite-muscovite, 43 % Qtz, 21% feldspar, 6% calcite, and 4% chlorite-kaolinite. It is from the same outcrop as the "Gaunt Creek Scarp Gouge U3" sample reported in Boulton et al., 2012.

The fault-zone in the Cataclasite Creek site is eroded by the creek flow. The sample was collected from the bottom of a creek bed after blocking the water flow (Fig. 12). The blue-green gouge was incohesive and water saturated. The XRD composition of

this sample is 44% illite-muscovite, 17% quartz, 24% feldspar, 4% calcite, 11% chlorite-kaolinite.

The Waikukupa Creek sample is located on the Waikukupa Thrust, which is an abandoned fault trace. The exposure is a 5-7 m tall loosely consolidated cliff (Fig. 12) along a washout of Waikukupa creek. A 10-15 mm grey-blue gouge layer was located and collected. The sample contained 29% illite-muscovite, 23% quartz, 19% Feldspar, 12% calcite, and 17% chlorite-kaolinite. This sample is from the same outcrop as the "Waikukupa River U3" gouge reported in Boulton et al., 2012.

The XRD analyses were performed in the lab of Dr. Andrew Elwood-Madden at the University of Oklahoma by using the Rigaku Ultima IV diffractometer with Bragg-Brentano geometry and a Cu X-ray.

Figure 11. Location map of the sample collection sites and the DFDP-2 borehole.

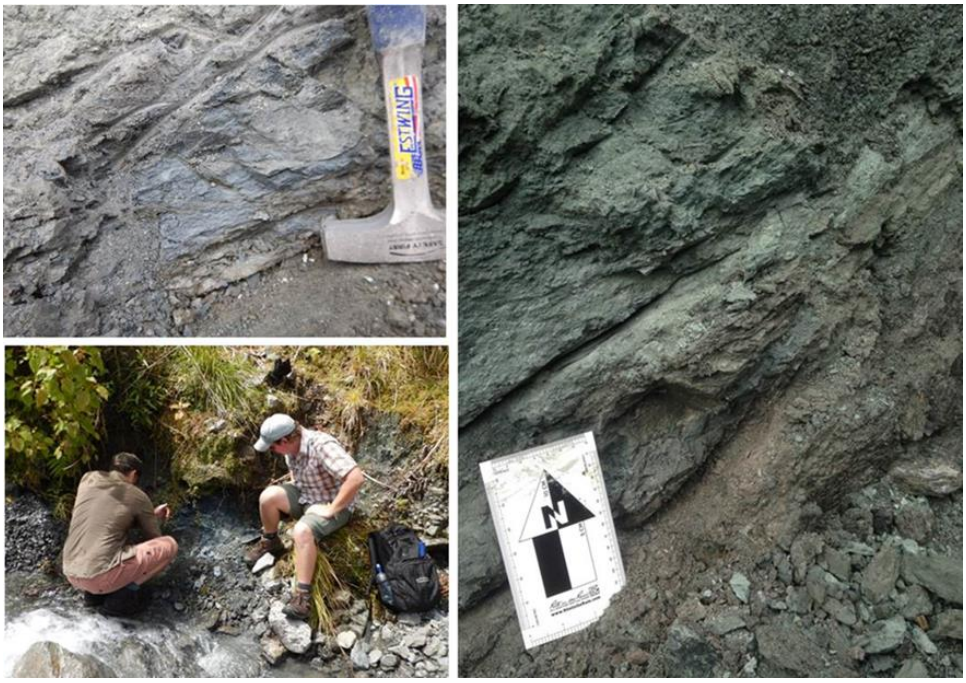

Figure 12. Photos of three sampling locations Top Left: Photo shows the sample at Gaunt Creek before collection Bottom Left: shows the gouge before collection located at Waikukupa Creek. Right: shows collection of the unconsolidated gouge from Cataclasite Creek.

TESTING GOUGE AT SEISMIC CONDITIONS

I performed sixteen experiments on the three fault gouges under similar conditions (Table 4) of: (1) natural gouge dampness; (2) normal stress of σ_n ~3 MPa; and (3) velocity range of 0.002 to 1.5 m/s. All experiments were run as stepped velocity, each experiment with six steps in two cycles of similar velocity steps (Fig. 13). The experiments were divided into were three velocity ranges (Table 4):

1. Low: 0.002-0.02 m/s with 1 cm slip-distance in each step (Fig. 13A).
2. Medium: 0.02-0.2 m/s with 14 cm slip-distance in each step (Fig. 13B)
3. High: 0.2-0.74 m/s with 1.5 m slip-distance in each step (Fig. 13C). In one run (4078) the highest velocity was 1.5 m/s.

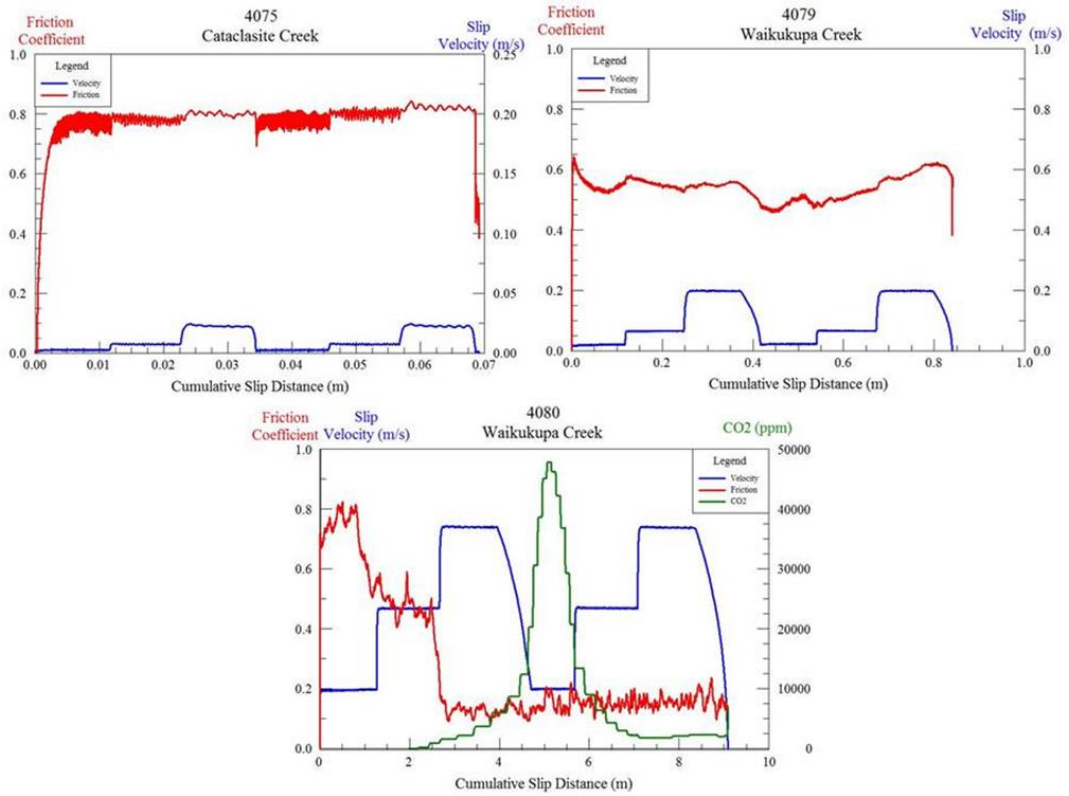

Figure 13. Friction coefficient (red) and slip-velocity (blue) in stepped-velocity experiments on Alpine Fault gouge; note scale differences between plots; . A. Stepping velocity in range 0.002-0.02 m/s. B. Stepping velocity in range of 0.02 to 0.2 m/s. C. Stepping velocity in range of 0.2 to 0.74 m/s.

EXPERIMENTAL RESULTS: FRICTIONAL STRENGTH

The mineralogical analyses of the samples indicated that the samples have similar compositions. As this is the case, it is expected that the frictional behavior of the three gouge samples will be less affected by composition and more affected by slip-velocity and slip-distance. Accordingly, I describe below the results of the experiments in terms of the loading velocities.

Low Velocity

At low velocity, all samples show frictional strengths above $\mu = 0.50$, typically around $\mu = \sim 0.65$. The sample from Cataclasite Creek was consistently samples the strongest, with μ values of 0.77 and higher. The strength of the samples evolves during

the velocity stepping procedure in similar ways. Initially, they exhibit slip strengthening or neutral behavior (Fig. 14A, B) until a velocity of 0.02 m/s and then show some slip weakening. In the case of the sample from Cataclasite Creek, it shows velocity strengthening behavior over the entire velocity range (Fig. 14C). The observed behavior in the first sequence of velocity steps, as described above, is then seen again in the second sequence of velocity steps (Fig. 14A-C). The low velocity experiments generate no to little temperature increase and no CO_2 emission (Table 4).

Medium Velocity

Over the medium velocity range, samples from Gaunt Creek and Waikukupa Creek show similar values for frictional strength, μ =0.60-0.70 (Fig 15A,B). The sample from Cataclasite Creek was weaker over the entire velocity range. This sample exhibited an initial value of μ = 0.55 and proceeded to slip weaken throughout the experiment (Fig. 15C). The behavior of samples from Gaunt Creek and Waikukupa Creek were fairly consistent over the entire velocity range, showing only gentle trend of strengthening and weakening (Fig. 15A,B). All samples showed a temperature rise of 10-20 ° C by the end of the experiment (Table 4). The Gaunt Creek sample showed a distinct peak in CO_2 emission of 27,500 ppm, about 20 seconds after the experiment ended (Fig. 15A). Samples from Waikukupa Creek and Cataclasite Creek showed small values of CO_2 emission, but remained below the vacuum level (Table 4).

Fast and Very Fast Velocities

In the fast velocity experiments, all samples showed an initial strengthening trend that changed to a drastic weakening trend once a velocity of 0.46 m/s was attained (Fig. 16A-C). Initial values of friction between μ=0.6-0.8, during the initial velocity of 0.2 m/s) weakened dramatically to values of $\mu \leq 0.3$ and remained there for the rest of the

experiment, regardless of velocity changes (Fig. 16A-C). An additional experiment, over a very fast velocity range, was performed on the sample from Cataclasite Creek (Fig. 16D). This experiment showed at steady frictional strength of μ ~0.8 at a velocity of 0.2 m/s that weakened to $\mu = 0.25$ at a velocity of 0.46 m/s. The sample remained weak throughout the rest of the experiment (Fig. 16D). In all experiments at these velocities, temperature rises greater than or equal to 30°C were observed along significant emissions of CO_2 (greater than 50,000 ppm; Table 4). In most cases, the apparent saturation of CO_2 at 50,000 ppm is an artifact of the limit set on the measurement device before the experiment. Actual values of CO_2 emission were higher. Emissions of CO_2 usually peaked, with a second delay, after the first instance of the velocity 0.74 m/s, and then again after the second occurrence. Temperature rise during the very fast velocity experiment was not measured due to a thermocouple malfunction.

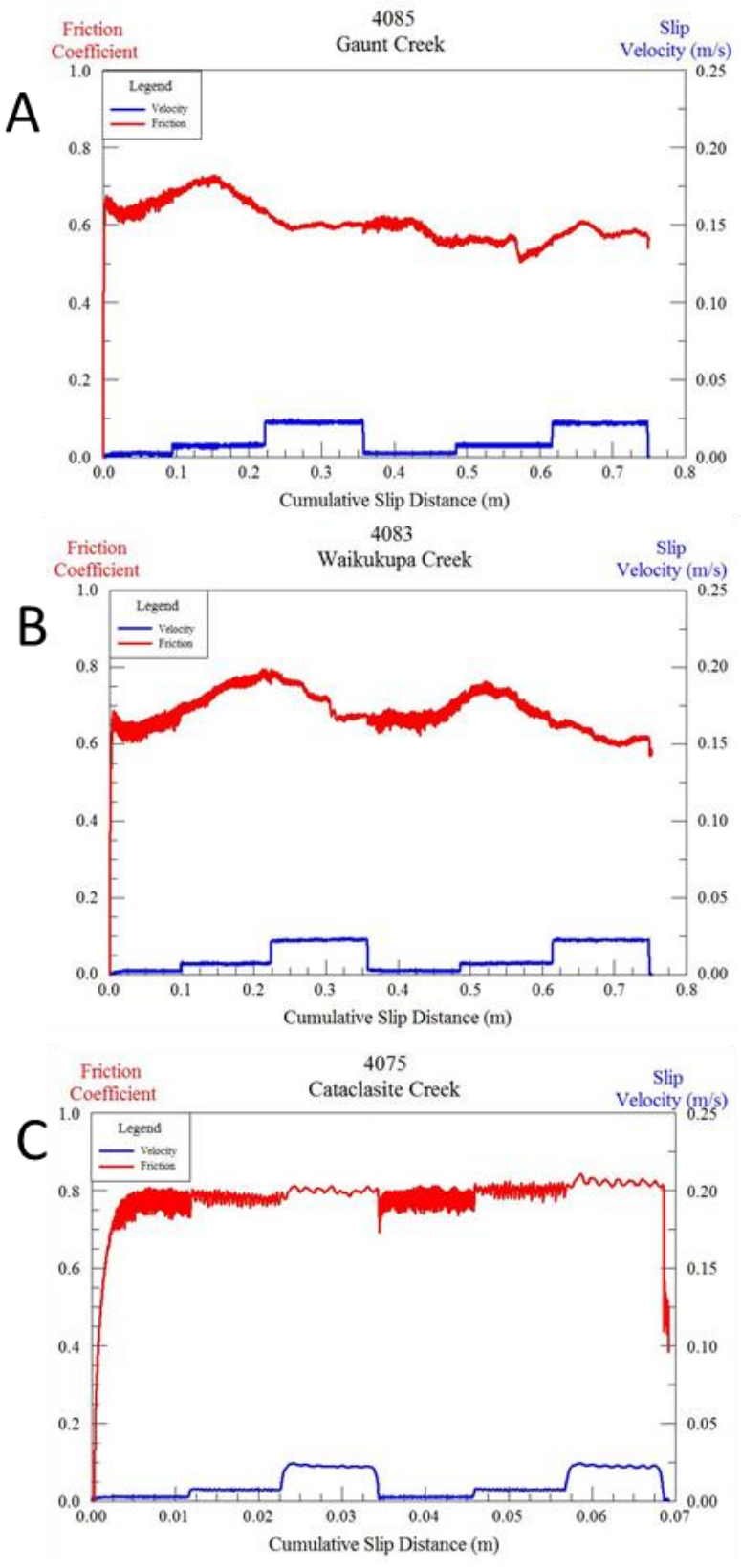

Figure 14. "Low" velocity experiments for all three samples.

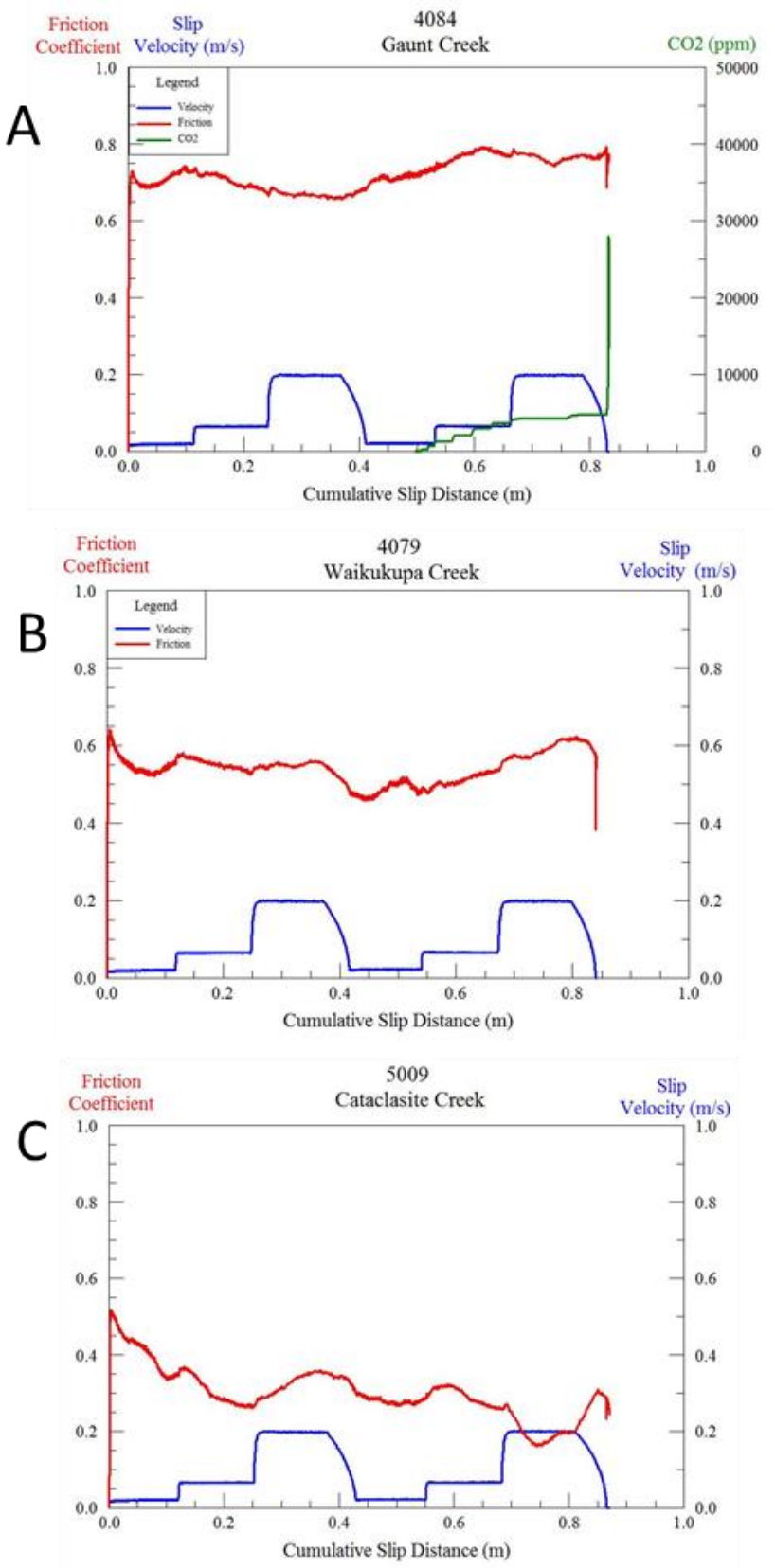

Figure 15. ”Medium” velocity experiments for all three samples.

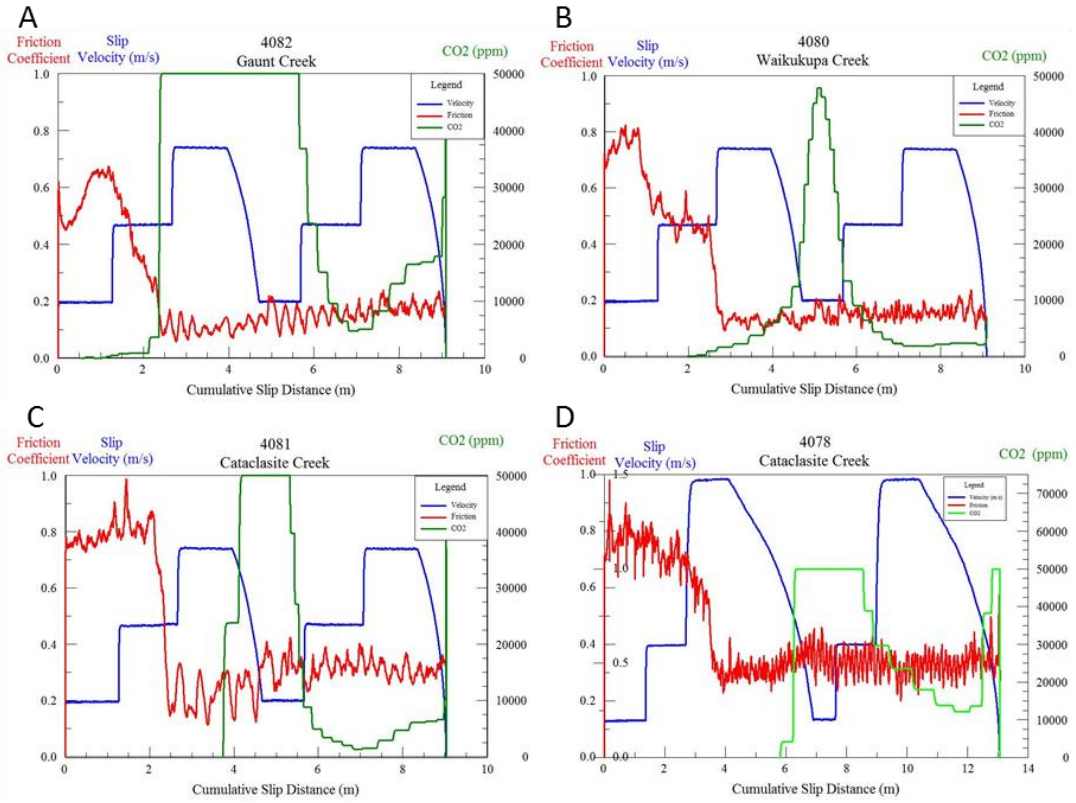

Figure 16. (A-C) "Fast" velocity experiments for all three experimental samples. (D) "Very fast" velocity experiment for the sample from Cataclasite Creek.

Table 4. Experimental conditions (left seven columns) and main responses (right three columns

Sample	Run	Velocity (m/s)			σn	Total Displacement (m)	Velocity	Comp	Temp. rise	CO_2
		Step 1 & 4	Step 2 & 5	Step 3 & 6			Description	(μm)	(C)	(ppm)
Cataclasite Cr.	4075	0.002	0.007	0.02	2.2	0.14	low	900	NA	NA
Cataclasite Cr.	4077	0.002	0.007	0.02	2.8	0.75	low	870	NA	NA
Cataclasite Cr.	4078	0.2	0.75	1.5	3	13.1	very fast	700	NA	50000*
Waikukupa Cr.	4079	0.02	0.065	0.2	3	0.84	medium	400	10	NA
Waikukupa Cr.	4080	0.2	0.46	0.74	3	9.1	fast	600	50	47810
Cataclasite Cr.	4081	0.2	0.46	0.74	3	9	fast	600	85	50000*
Gaunt Cr.	4082	0.2	0.46	0.74	3	9.1	fast	800	30	50000*
Waikukupa Cr.	4083	0.002	0.007	0.02	3	0.75	low	500	NA	NA
Gaunt Cr.	4084	0.02	0.065	0.2	3	0.83	medium	680	13	27480
Gaunt Cr.	4085	0.002	0.007	0.02	3	0.75	low	600	4	NA
Cataclasite Cr.	5009	0.02	0.065	0.2	3	0.87	medium	300	7	NA
Cataclasite Cr.	5010	0.02	0.065	0.2	3	1.74	medium	80	5	NA
Cataclasite Cr.	5011	0.02	0.065	0.2	3	4.1	medium	150	21	116
Cataclasite Cr.	5012	0.02	0.065	0.2	3	6.6	medium	20	23	248

**highest value recorded before becoming saturated due to a maximum value set too low before the experiment took place*

SYNTHESIS OF EXPERIMENTAL RESULTS

Friction vs Velocity

Synthesis of the experimental results consisted in breaking down each experiment by the sample type, slip-velocity, and total displacement. An average friction coefficient with standard deviation was calculated for each velocity step. Fig. 17 displays a drastic weakening at velocity of 0.3-0.4 m/s in the first velocity cycle, and they remained weak at the higher velocities (Fig. 16). During the second cycle of velocity steps, the value is lowered to 0.2 m/s, which is the result of the sample remaining in a weakened state from the first cycle of velocity steps, in the “fast” velocity experiments.

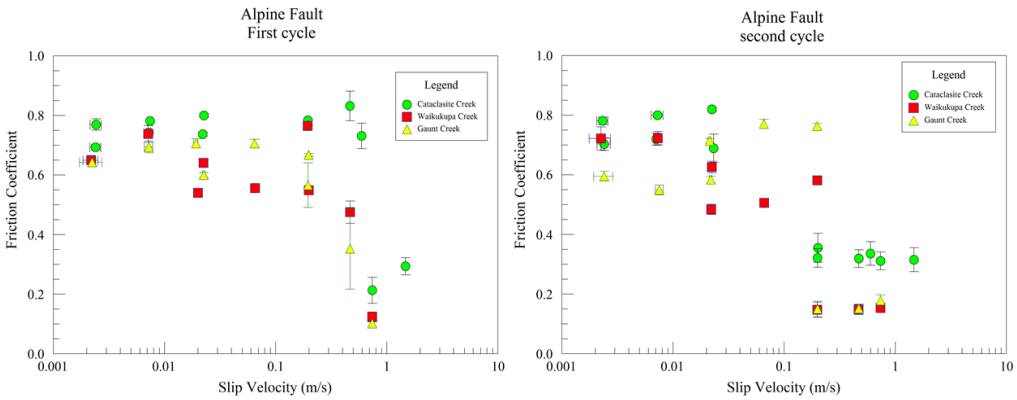

Figure 17. The synthesized average steady state friction coefficients for three separate samples. Left: first cycle of stepped velocity runs. Right: Second cycle of stepped velocity runs.

Friction vs Displacement

The plot of all experiments with significant weakening (Fig. 18) indicate that weakening occurred after slip to a critical distance of 2-4 m at slip-velocity > 0.2 m/s.

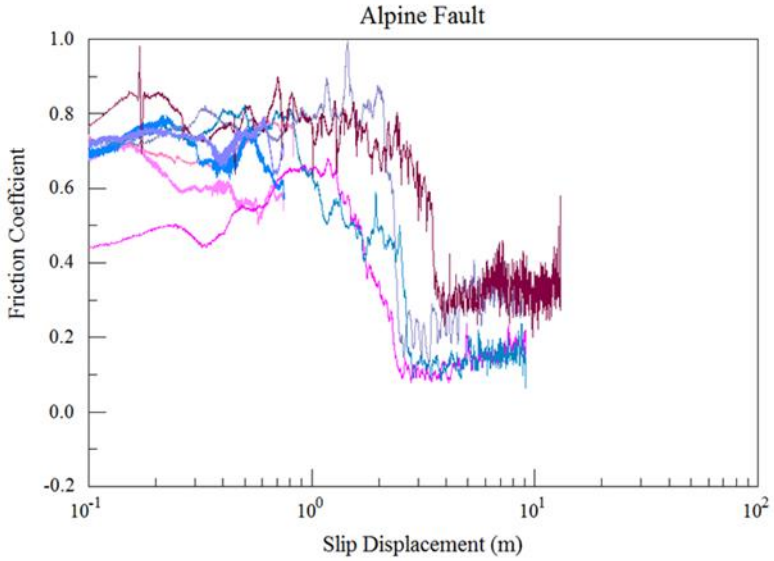

Figure 18. Friction coefficient evolution with respect to cumulative slip distance for 7 highest velocity experiments (V > 0.2 m/s).

Friction Maps

As the friction coefficients dependent on both slip-velocity and slip-displacement, the results are displayed on friction maps for each velocity step cycle (Fig. 19-20). In both cycles, samples at high velocity (> 0.2 m/s) and large-displacements (> 2 m) show

significant weakening (Fig. 19). The friction map of cycle 2 (Fig. 20) reinforces above observation that once the sample becomes weakened, it remains weak.

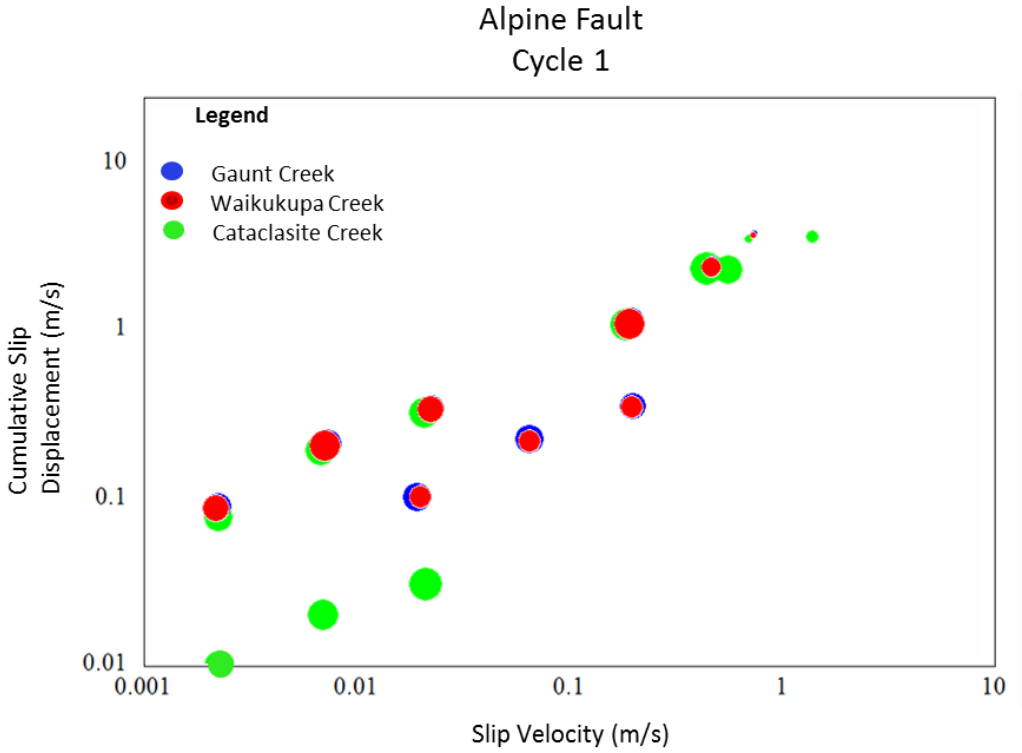

Figure 19. Friction map for our experimental samples shown for velocity cycle 1.

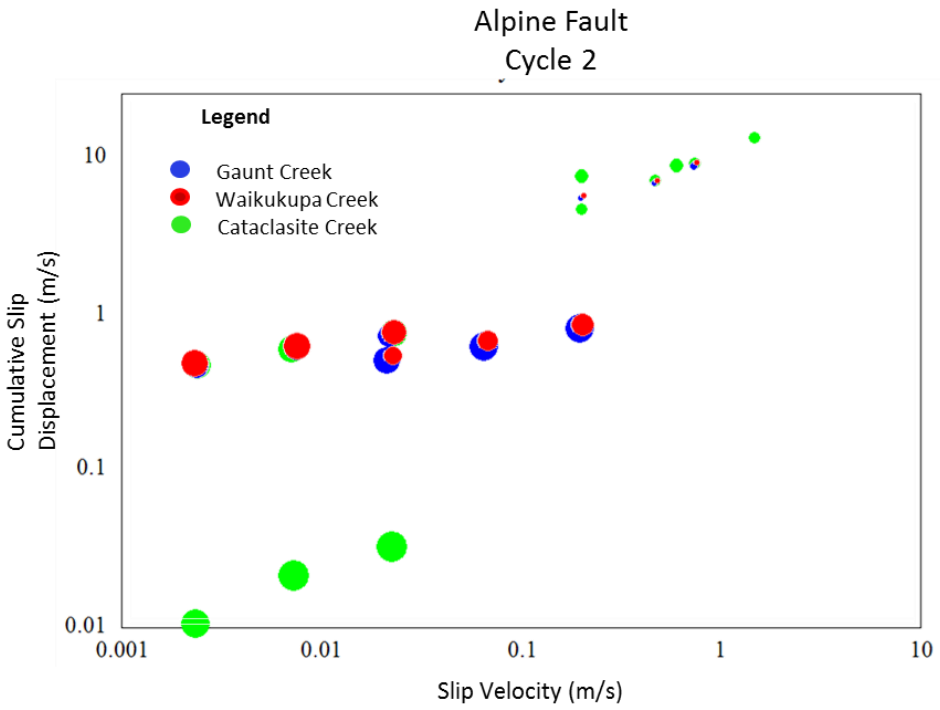

Figure 20. Friction Map for our experimental samples shown for velocity cycle 2.

MICROSCOPIC OBSERVATIONS

The gouge samples were examined after the experiment macroscopically and with SEM. The macroscopic structure was significantly different after three runs of low, medium and high velocity loading styles (Fig. 22).

1. Low velocity displays rough, irregular slip surface with limited localization.
2. Medium velocity displays multiple, relatively smooth surfaces with clear slickenlines.
3. Fast velocity displays shiny, hard smooth primary slip surface with secondary (probably earlier) surfaces.

Similar observations were observed in high-velocity shear experiments of pure calcite by Smith et al. (2015).

The SEM images support the above macroscopic observations and further indicate that:

1. Calcite crystals (rhombic cleavage, Fig. 23A) remained unaltered (no thermal decomposition) 100 µm from the primary slip surface along with a gradational grain size distribution, cataclasis near the slip surface and preservation of original size of the quartz grains further away (Fig. 23B).
2. Distributed shear along multiple surfaces were seen in a cross-section of the fault zone and smooth slip surfaces. (Fig. 23C, D)

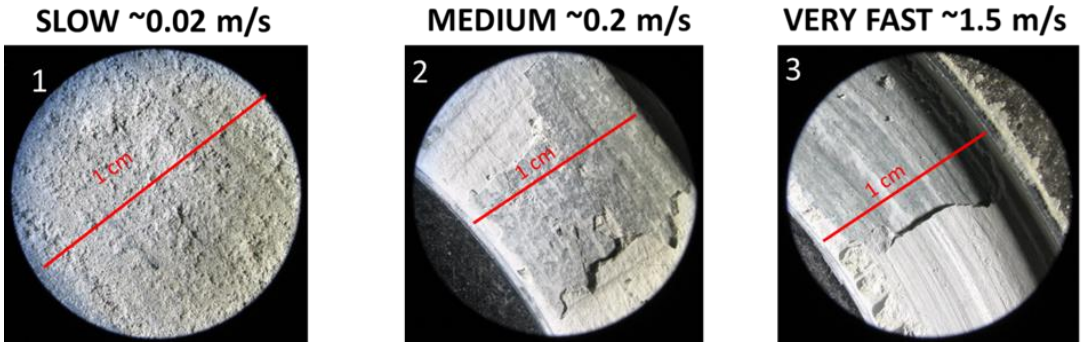

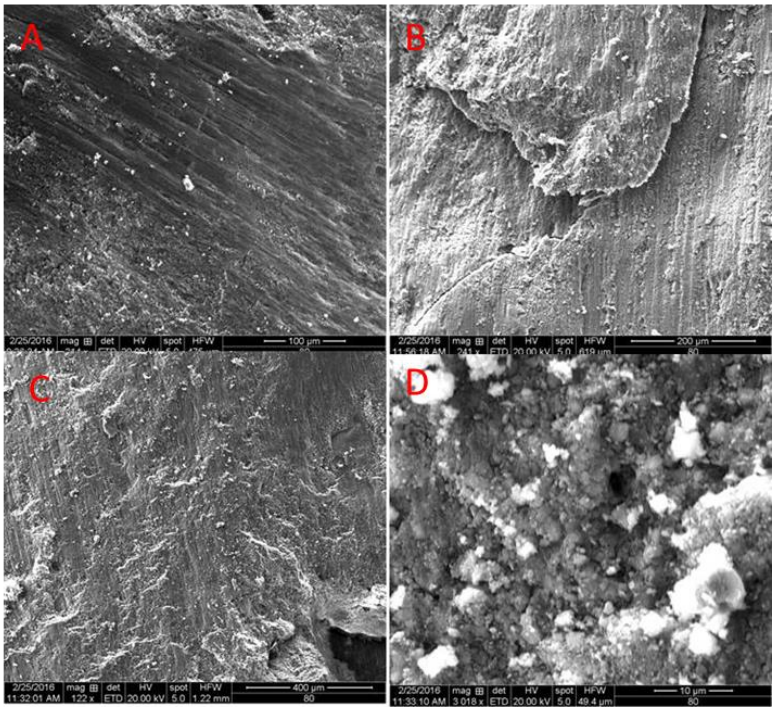

Figure 21. SEM images from the slip surface of sample 4076. Note the slickenlines indicating the direction of slip in photo A,B,and C. Photo D is a closer look and the above mentioned "smooth" surfaces showing particle aggregates.

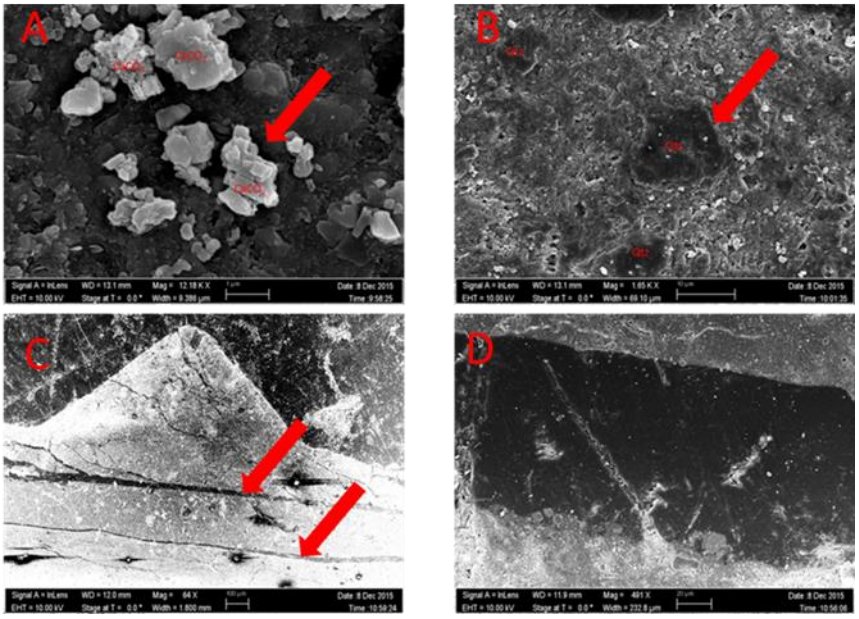

Figure 22. SEM photos of Alpine Fault gouge post experimentation. (A) Preserved calcite crystals (B)Preserved original grain size of quartz (C) Cross-section displaying distributed shear along multiple surfaces (D) Relatively smooth surface (epoxy is black material, sample is grey).

DISCUSSION

The present shear experiments on the Alpine Fault gouge revealed several significant features that are briefly discussed below.

1. The Alpine Fault gouge showed drastic dynamic weakening at slip velocity higher than 0.2 m/s (Fig. 17), and after slip-distance of 2-4 m (Fig. 18). While similar observations were made previously (e.g., diToro et al., 2011), the Alpine Fault gouge shows no clear sign of regaining strength (or healing) once the velocity decreases (Figs. 16C, D). If this behavior prevails under natural conditions, in could inhibits the development of the proposed self-healing slip pulse (Heaton, 1990; Perrin, 1995)
2. The intense CO_2 emission at high-velocities (Fig. 16) and the SEM images indicates that the presence of 6-12% of calcite strongly affected the friction evolution.
3. The present results for slip-velocity higher than 1 cm/s show gentle velocity strengthening at V <10 cm/s (Fig. 17). This observations are in excellent agreement (Fig. 24) with experiments of very low slip-velocity of V < 300 μm/s that were conducted on the Alpine Fault gouge in direct shear experiment in INGV laboratory, Rome. These experiments were kindly conducted by Marco Scuderi of INGV following our request.

4. A series of experiments on Cataclasite Creek gouge at medium velocity cycling (Fig. 25) was extended to large cumulative slip distances (Fig. 25). The gouge weakened during the first cycle, but displayed consistent strengthening afterward. The temperatures rise in this experiments suggest that gouge dehydration could lead to the observed strengthening as proposed for talc experiments (Chen et al., in progress).

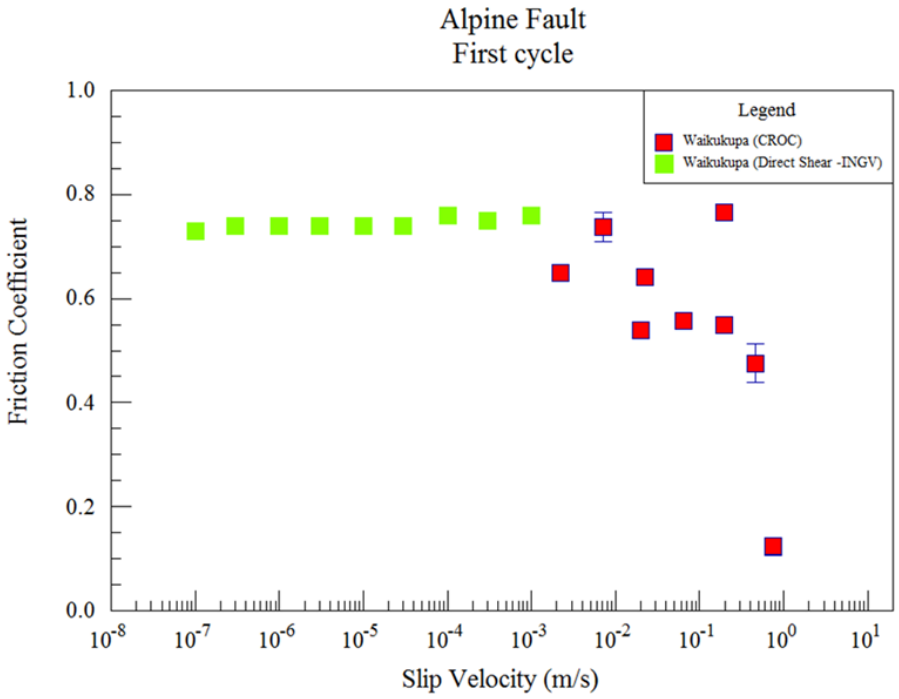

Figure 23. Comparison of the present friction results (first cycle only) with results run using direct shear (INGV, Rome, Italy) for room-dry samples of Waikukupa Creek sites. Their low velocity experiments show similar trend of slight velocity-strengthening also seen in the presented low CROC experiments before weakening at the approach of seismic velocity.

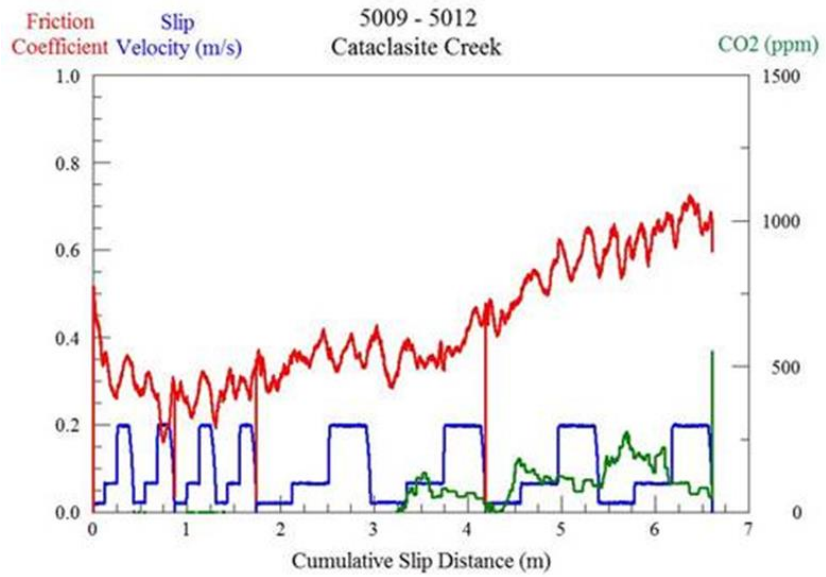

Figure 24. Results from four (two cycles each) continuous experiments (5009-5012) in which dehydration of the sample occurs and results in significant strengthening of the gouge.

SUMMARY

Experiments performed over a large velocity range, including seismic slip velocities, on the three fault gouges collected from surface exposures in New Zealand resulted in the following conclusions:

1. At short slip displacements and low slip velocities, Friction coefficients of 0.68 to 0.75 occur for all three Alpine Fault gouges with slight velocity strengthening (Fig. 19).
2. There is profound dynamic weakening over a small range of slip velocities (0.2-0.4 m/s), leading to steady-state friction coefficient of ~0.1-0.33 (Fig. 18).
3. Once the sample has weakened, no recovery of frictional strength occurs even at low slip velocities (Fig. 20).
4. This general behavior is similar to the experimentally observed results observed along carbonate faults suggesting that the calcite in the gouges (~6-12%) exerts significant control over the global behavior of the gouge.

5. The microstructural analysis indicates distributed shear over multiple surfaces with very fine grains at these surfaces. Original grain size is preserved further from slip surface, indicating that most of the shear was localized and accommodated along these surfaces (Fig. 23).
6. The composition of the fault gouge may enable fault rupture to reach the surface enhancing the damage to human-built structures.

References

Barnes, P.M., R. Sutherland, and J. Delteil. Strike-slip structure and sedimentary basins of the southern Alpine Fault, Fiordland, New Zealand. Geological Society of America Bulletin 117.3-4 (2005): 411-435.

Berryman, K., et al. Late Holocene rupture history of the Alpine fault in south Westland, New Zealand. Bulletin of the Seismological Society of America 102.2 (2012): 620-638.

Blanpied, M. L., D A. Lockner, and J D. Byerlee. Frictional slip of granite at hydrothermal conditions. Journal of Geophysical Research: Solid Earth 100.B7 (1995): 13045-13064.

Brace, W. F., and J. D. Byerlee. Stick-slip as a mechanism for earthquakes. Science153.3739 (1966): 990-992.

Boneh, Y., et al. Evolution of wear and friction along experimental faults. Pure and Applied Geophysics 171.11 (2014): 3125-3141.

Boneh, Y., A Sagy, and Z Reches. Frictional strength and wear-rate of carbonate faults during high-velocity, steady-state sliding. Earth and Planetary Science Letters 381 (2013): 127-137.

Boulton, C., et al. Physical properties of surface outcrop cataclastic fault rocks, Alpine Fault, New Zealand. Geochemistry, Geophysics, Geosystems 13.1 (2012).

Chang, J. C., D A. Lockner, and Z. Reches. Rapid acceleration leads to rapid weakening in earthquake-like laboratory experiments. Science 338.6103 (2012): 101-105.

Chen, X., et al. The frictional strength of talc gouge in high-velocity shear experiments In progress

Cooper, A. F., and R. J. Norris. Estimates for the timing of the last coseismic displacement on the Alpine Fault, northern Fiordland, New Zealand. New Zealand journal of geology and geophysics 33.2 (1990): 303-307.

De Pascale, G. P., Neotectonics and Paleoseismology of the Central Alpine Fault, New Zealand. (2014).

Dieterich, J. H. Constitutive properties of faults with simulated gouge. Mechanical behavior of crustal rocks: the Handin volume (1981): 103-120.

Ellsworth, W L. Injection-induced earthquakes. Science 341.6142 (2013): 1225942

Faulkner, D. R., et al. Stuck in the mud? Earthquake nucleation and propagation through accretionary forearcs. Geophysical Research Letters 38.18 (2011).

Harris, R. A., and S M. Day. Dynamic 3D simulations of earthquakes on en echelon faults. Geophysical Research Letters 26.14 (1999): 2089-2092.

Healy, J. H., et al. The denver earthquakes. Science 161.3848 (1968): 1301-1310.

Heaton, T. H. Evidence for and implications of self-healing pulses of slip in earthquake rupture. Physics of the Earth and Planetary Interiors 64.1 (1990): 1-20.

Hirose, T., and T Shimamoto. Growth of molten zone as a mechanism of slip weakening of simulated faults in gabbro during frictional melting. Journal of Geophysical Research: Solid Earth (1978–2012) 110.B5 (2005).

Ikari, M. J., D M. Saffer, and C Marone. Frictional and hydrologic properties of clay-rich fault gouge. Journal of Geophysical Research: Solid Earth 114.B5 (2009).

Ikari, M. J., et al. Frictional strength, rate-dependence, and healing in DFDP-1 borehole samples from the Alpine Fault, New Zealand. Tectonophysics 630 (2014): 1-8.

Jaeger, J.C., NGW Cook, and R Zimmerman. Fundamentals of rock mechanics. John Wiley & Sons, 2009.

Kanamori, H. Mechanics of earthquakes. Annual Review of Earth and Planetary Sciences 22 (1994): 207-237.

Keranen, K. M., et al. Potentially induced earthquakes in Oklahoma, USA: Links between wastewater injection and the 2011 Mw 5.7 earthquake sequence. Geology 41.6 (2013): 699-702.

Kitajima, H, et al. "High-speed friction of disaggregated ultracataclasite in rotary shear: Characterization of frictional heating, mechanical behavior, and microstructure evolution." Journal of Geophysical Research: Solid Earth 115.B8 (2010).

Kohli, A. H., and M D. Zoback. Frictional properties of shale reservoir rocks. Journal of geophysical research: solid earth 118.9 (2013): 5109-5125.

Liao, Z, J C. Chang, and Z Reches. Fault strength evolution during high velocity friction experiments with slip-pulse and constant-velocity loading. Earth and Planetary Science Letters 406 (2014): 93-101.

Little, T. A., R. J. Holcombe, and B. R. Ilg. Ductile fabrics in the zone of active oblique convergence near the Alpine Fault, New Zealand: identifying the neotectonic overprint. Journal of Structural Geology 24.1 (2002): 193-217.

Lupini, J. F., A. E. Skinner, and P. R. Vaughan. The drained residual strength of cohesive soils. Geotechnique 31.2 (1981): 181-213.

McNamara, D. E., et al. Efforts to monitor and characterize the recent increasing seismicity in central Oklahoma. The Leading Edge 34.6 (2015): 628-639.

McNamara, D. E., et al., 2015, Earthquake Hypocenters and Focal Mechanisms in Central Oklahoma Reveal a Complex System of Reactivated Subsurface Strike-Slip Faulting, AGU Geophysical Research Letter, 10.1002/2014GL062730

Moore, D. E., and D A. Lockner. Crystallographic controls on the frictional behavior of dry and water-saturated sheet structure minerals. Journal of Geophysical Research: Solid Earth 109.B3 (2004).

Moore, D. E., and M J. Rymer. Talc-bearing serpentinite and the creeping section of the San Andreas fault. Nature 448.7155 (2007): 795-797.

Norris, R. J., and A F. Cooper. Late Quaternary slip rates and slip partitioning on the Alpine Fault, New Zealand. Journal of Structural Geology 23.2 (2001): 507-520.

Petersen, M. D., et al. 2016 One-Year Seismic Hazard Forecast for the Central and Eastern United States from Induced and Natural Earthquakes. No. 2016-1035. US Geological Survey, 2016.

Perrin, G., J R. Rice, and G Zheng. Self-healing slip pulse on a frictional surface. Journal of the Mechanics and Physics of Solids 43.9 (1995): 1461-1495.

Reches, Z., and D A. Lockner. Fault weakening and earthquake instability by powder lubrication. Nature 467.7314 (2010): 452-455

Segall, P. Earthquakes triggered by fluid extraction. Geology 17.10 (1989): 942-946.

Walsh, F. R., and M D. Zoback. Oklahoma's recent earthquakes and saltwater disposal. Science advances 1.5 (2015): e1500195.

Sutherland, R., et al. Do great earthquakes occur on the Alpine Fault in central South Island, New Zealand? A Continental Plate Boundary: Tectonics at South Island, New Zealand (2007): 235-251.

Townend, J., R. Sutherland, and V. Toy (2009), Deep Fault Drilling Project—Alpine Fault, New Zealand, Sci. Drill., 8, 75–82, doi:10.2204/iodp.sd.8.12.2009.

Toy, V. G., et al. Thermal regime in the central Alpine Fault zone, New Zealand: Constraints from microstructures, biotite chemistry and fluid inclusion data. Tectonophysics 485.1 (2010): 178-192.

Wei, S., et al. The 2014 Mw 6.1 South Napa earthquake: A unilateral rupture with shallow asperity and rapid afterslip. Seismological Research Letters 86.2A (2015): 344-354.

Wells, A., et al. Prehistoric dates of the most recent Alpine fault earthquakes, New Zealand." *Geology* 27.11 (1999): 995-998.

Appendix A: Mechanical results – Reservoir rock and QCC

Appendix A is comprised of the mechanical results from each individual experiment ran on the reservoir rock and QCC material. The graphs are grouped for samples and composition mixtures and in numerical order from least to greatest. Each plot shows friction (left y-axis) and velocity (right y-axis) against cumulative slip-displacement

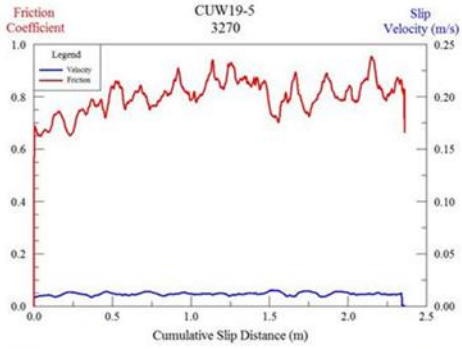

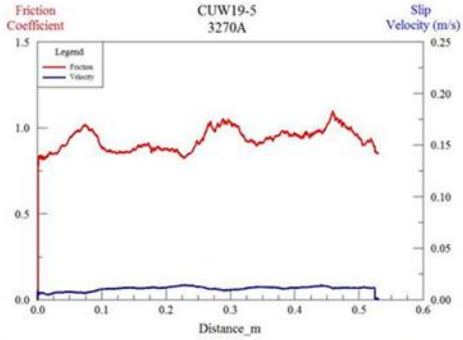

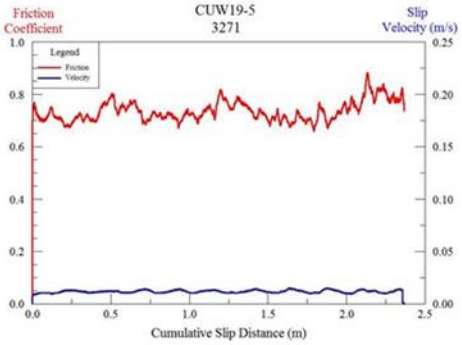

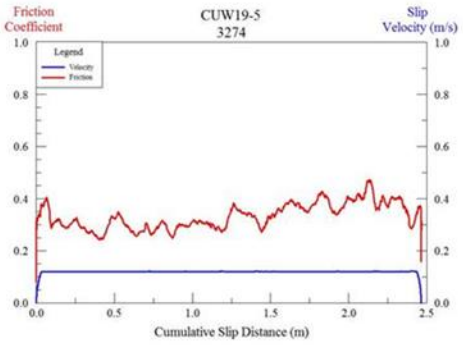

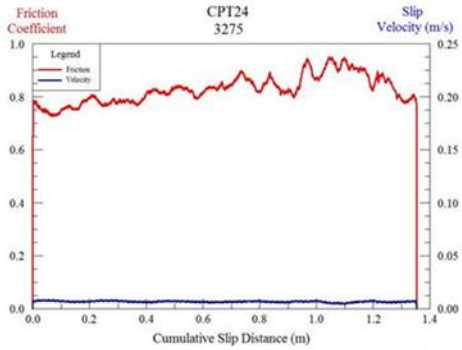

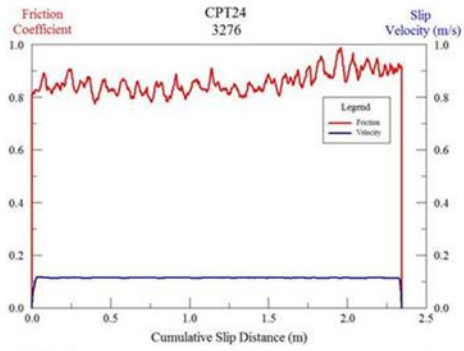

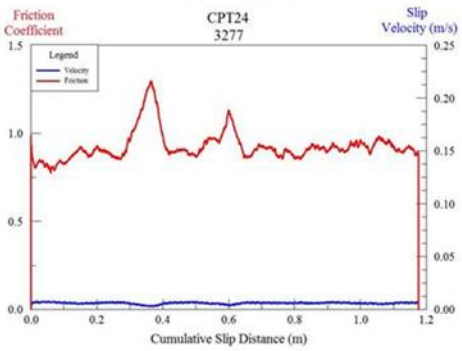

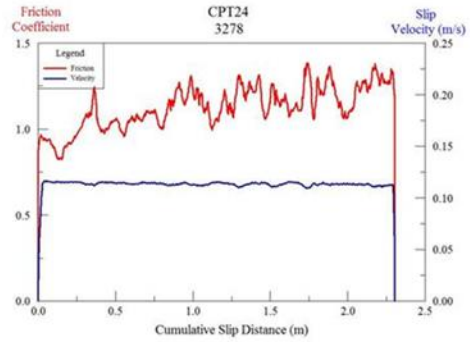

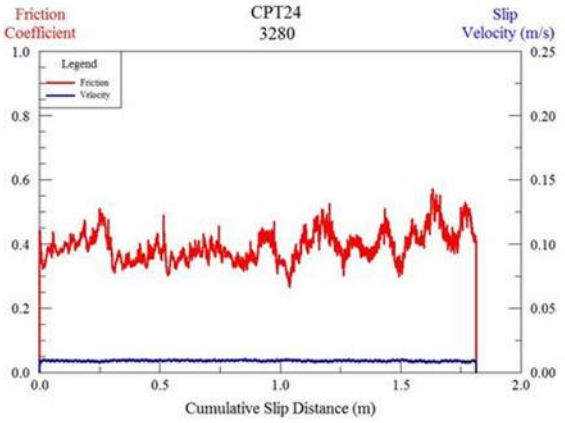
Friction Coefficient
CPT24
3280
Slip Velocity (m/s)
Legend
Friction
Velocity
Cumulative Slip Distance (m)

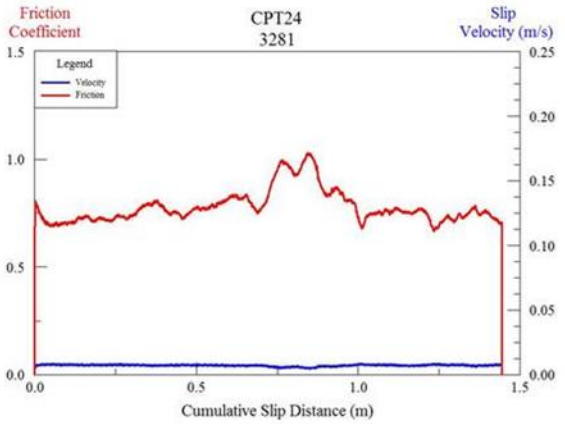
Friction Coefficient
CPT24
3281
Slip Velocity (m/s)
Legend
Velocity
Friction
Cumulative Slip Distance (m)

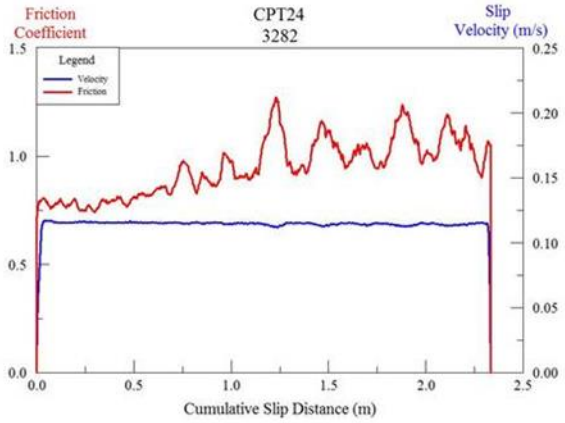
Friction Coefficient
CPT24
3282
Slip Velocity (m/s)
Legend
Velocity
Friction
Cumulative Slip Distance (m)

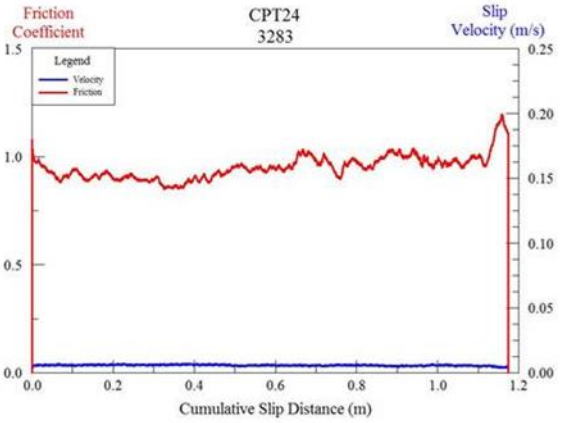
Friction Coefficient
CPT24
3283
Slip Velocity (m/s)
Legend
Velocity
Friction
Cumulative Slip Distance (m)

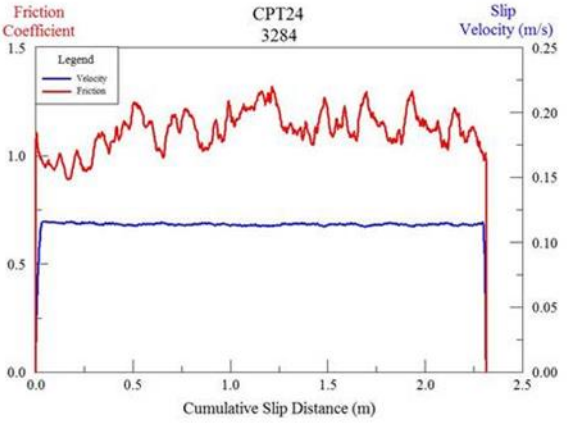
Friction Coefficient
CPT24
3284
Slip Velocity (m/s)
Legend
Velocity
Friction
Cumulative Slip Distance (m)

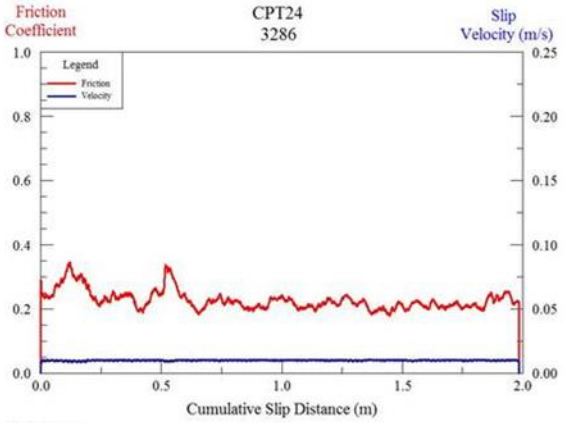
Friction Coefficient
CPT24
3286
Slip Velocity (m/s)
Legend
Friction
Velocity
Cumulative Slip Distance (m)

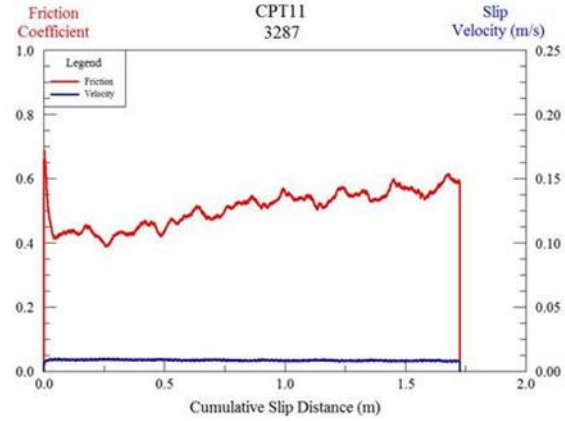
Friction Coefficient
CPT11
3287
Slip Velocity (m/s)
Legend
Friction
Velocity
Cumulative Slip Distance (m)

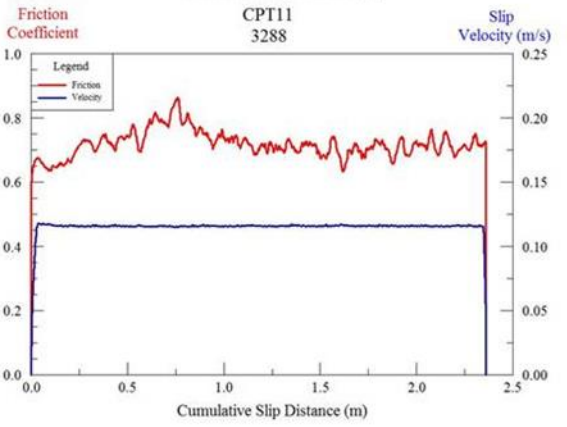
Friction Coefficient
CPT11
3288
Slip Velocity (m/s)
Legend
Friction
Velocity
Cumulative Slip Distance (m)

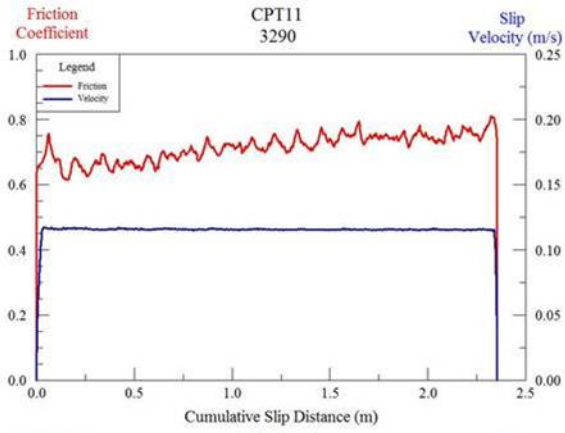
Friction Coefficient
CPT11
3290
Slip Velocity (m/s)
Legend
Friction
Velocity
Cumulative Slip Distance (m)

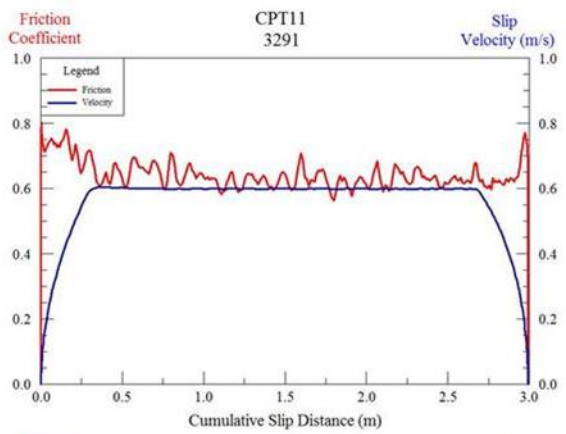
Friction Coefficient
CPT11
3291
Slip Velocity (m/s)
Legend
Friction
Velocity
Cumulative Slip Distance (m)

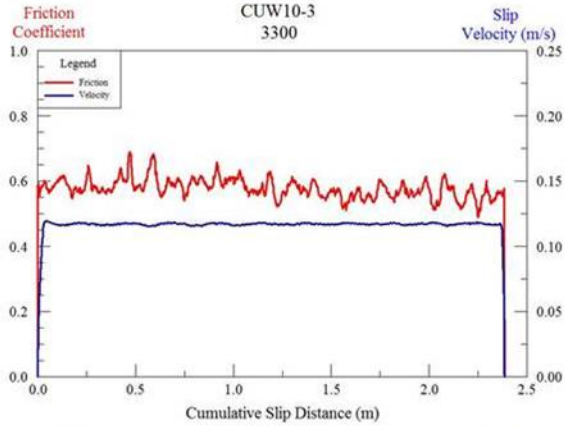
Friction Coefficient
CUW10-3
3300
Slip Velocity (m/s)
Legend
Friction
Velocity
Cumulative Slip Distance (m)

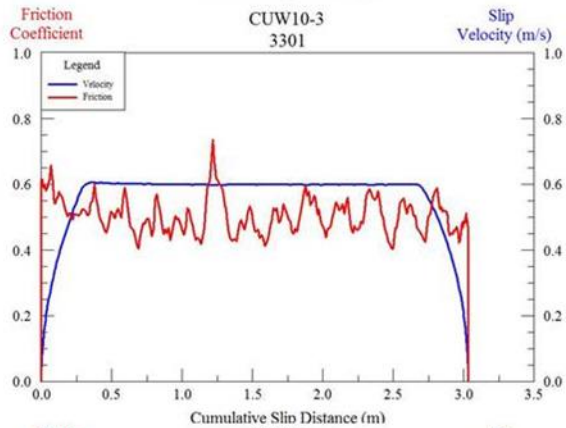
Friction Coefficient
CUW10-3
3301
Slip Velocity (m/s)
Legend
Velocity
Friction
Cumulative Slip Distance (m)

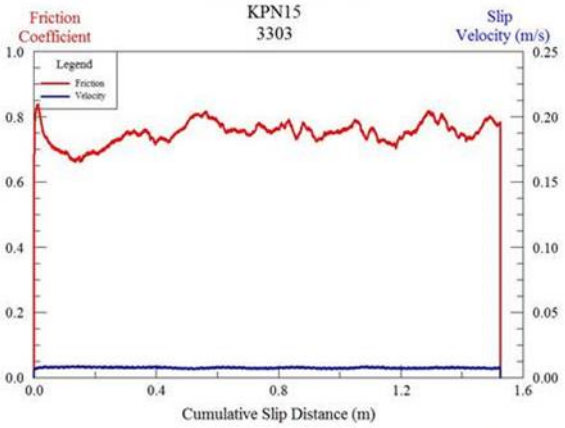
Friction Coefficient
KPN15
3303
Slip Velocity (m/s)
Legend
Friction
Velocity
Cumulative Slip Distance (m)

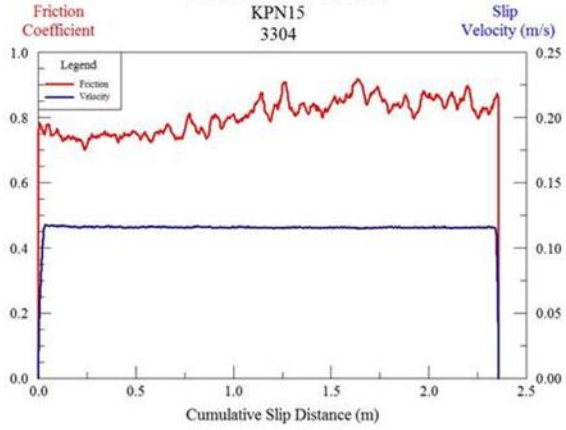
Friction Coefficient
KPN15
3304
Slip Velocity (m/s)
Legend
Friction
Velocity
Cumulative Slip Distance (m)

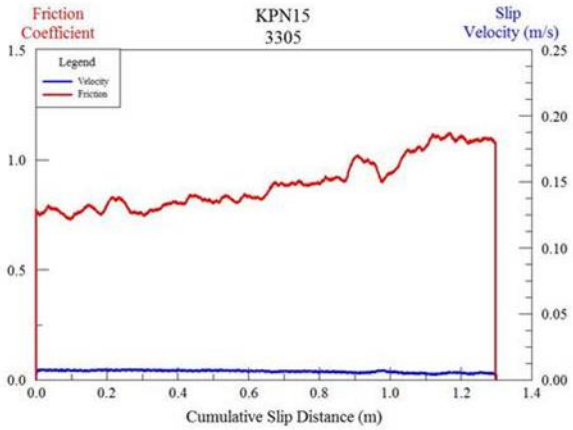
Friction Coefficient
KPN15
3305
Slip Velocity (m/s)
Legend
Velocity
Friction
Cumulative Slip Distance (m)

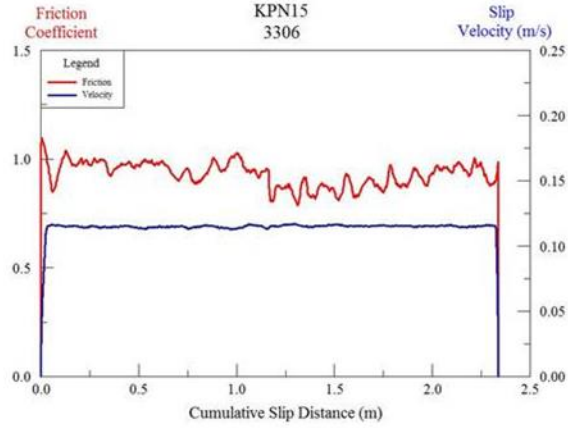
Friction Coefficient
KPN15
3306
Slip Velocity (m/s)
Legend
Friction
Velocity
Cumulative Slip Distance (m)

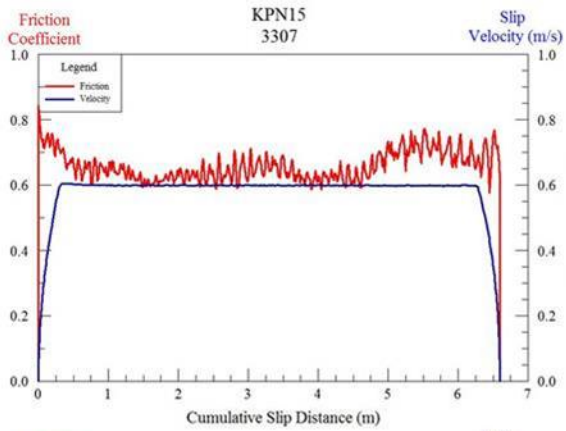
KPN15
3307
Friction Coefficient
Slip Velocity (m/s)
Legend
Friction
Velocity
Cumulative Slip Distance (m)

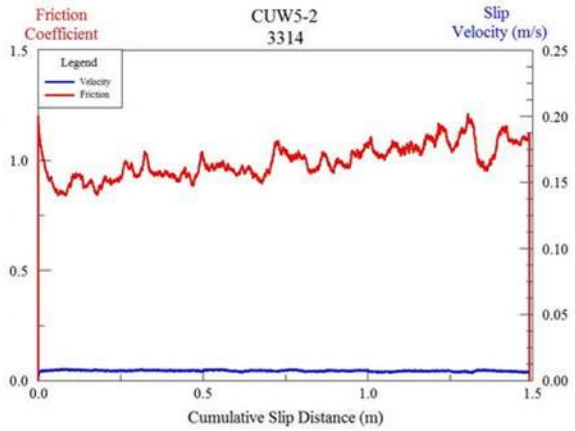
CUW5-2
3314
Friction Coefficient
Slip Velocity (m/s)
Legend
Velocity
Friction
Cumulative Slip Distance (m)

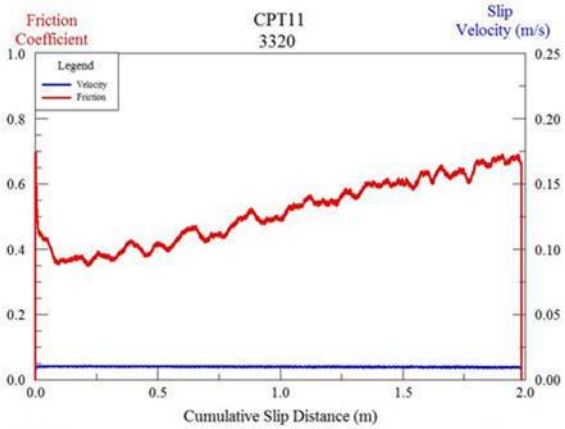
CPT11
3320
Friction Coefficient
Slip Velocity (m/s)
Legend
Velocity
Friction
Cumulative Slip Distance (m)

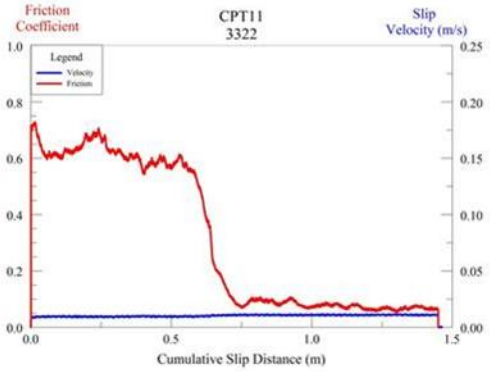
CPT11
3322
Friction Coefficient
Slip Velocity (m/s)
Legend
Velocity
Friction
Cumulative Slip Distance (m)

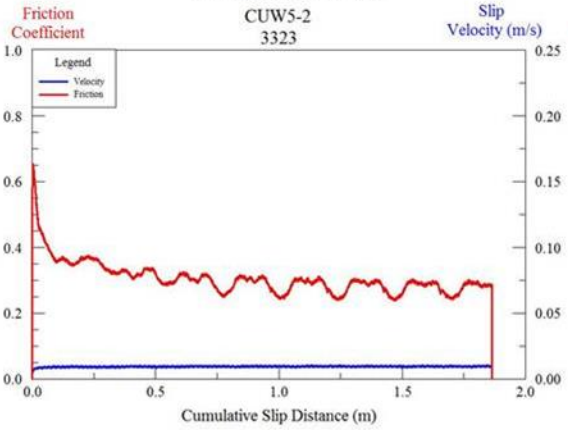
CUW5-2
3323
Friction Coefficient
Slip Velocity (m/s)
Legend
Velocity
Friction
Cumulative Slip Distance (m)

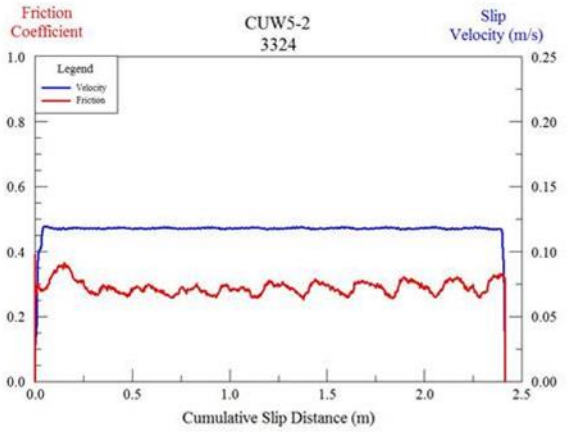
CUW5-2
3324
Friction Coefficient
Slip Velocity (m/s)
Legend
Velocity
Friction
Cumulative Slip Distance (m)

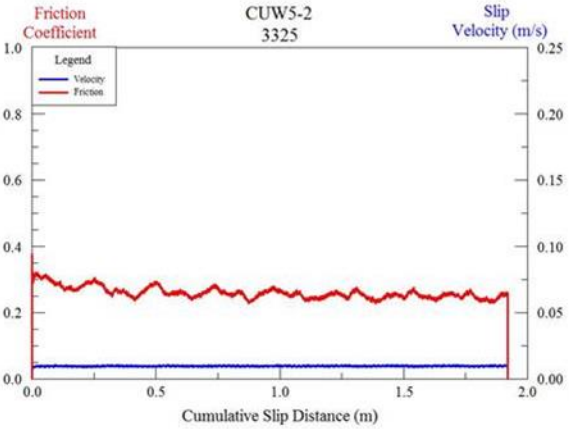
CUW5-2
3325
Friction Coefficient
Slip Velocity (m/s)
Legend
Velocity
Friction
Cumulative Slip Distance (m)

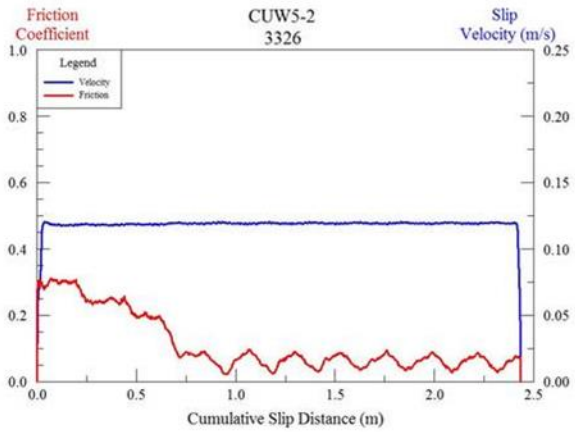
CUW5-2
3326
Friction Coefficient
Slip Velocity (m/s)
Legend
Velocity
Friction
Cumulative Slip Distance (m)

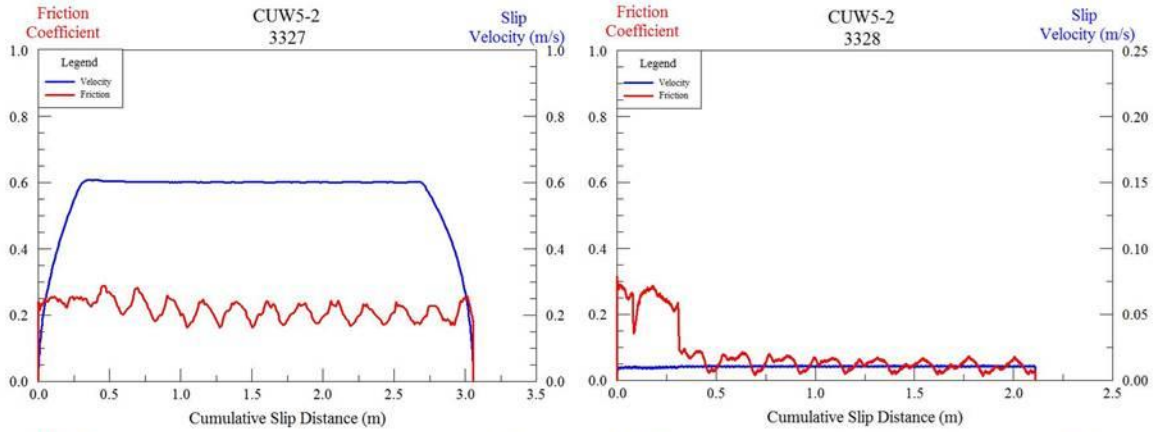
Friction Coefficient
CUW5-2
3327
Slip Velocity (m/s)
Legend
Velocity
Friction
Cumulative Slip Distance (m)

Friction Coefficient
CUW5-2
3328
Slip Velocity (m/s)
Legend
Velocity
Friction
Cumulative Slip Distance (m)

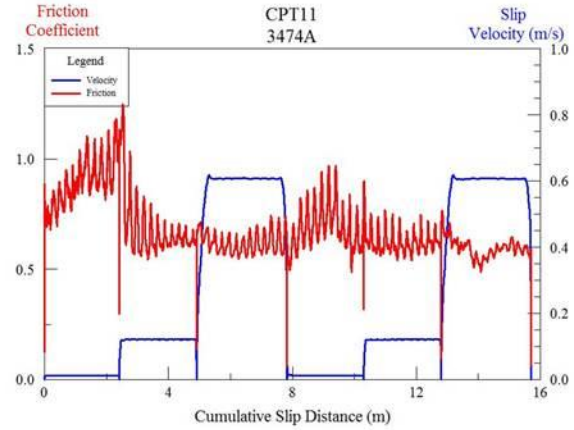
Friction Coefficient
CPT11
3474A
Slip Velocity (m/s)
Legend
Velocity
Friction
Cumulative Slip Distance (m)

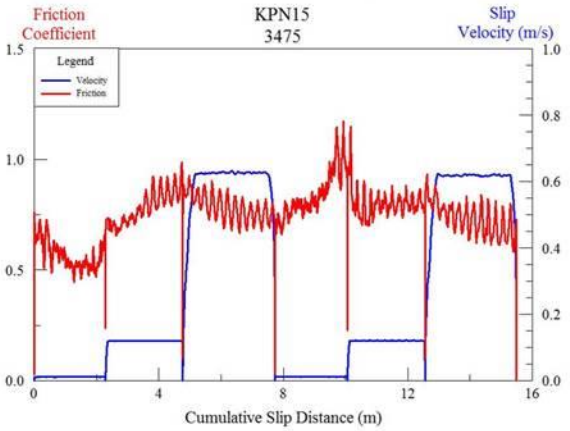
Friction Coefficient
KPN15
3475
Slip Velocity (m/s)
Legend
Velocity
Friction
Cumulative Slip Distance (m)

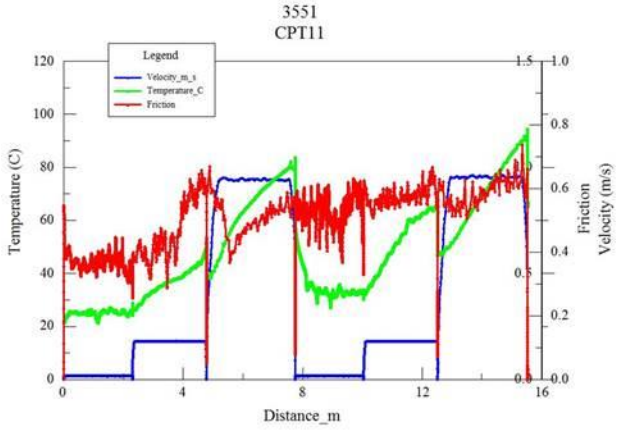
3551
CPT11
Legend
Velocity_m_s
Temperature_C
Friction
Temperature (C)
Friction Velocity (m/s)
Distance_m

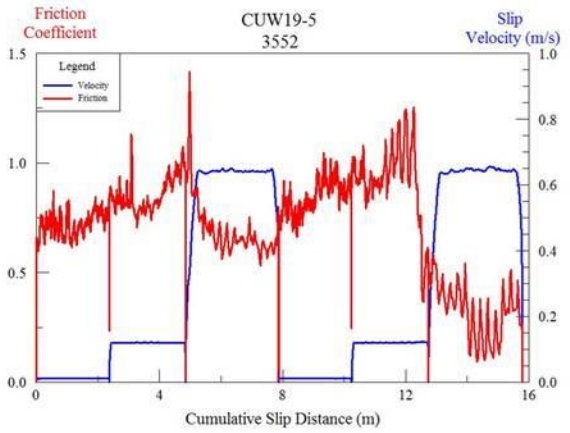
Friction Coefficient
CUW19-5
3552
Slip Velocity (m/s)
Legend
Velocity
Friction
Cumulative Slip Distance (m)

Appendix B: Synthesized Data

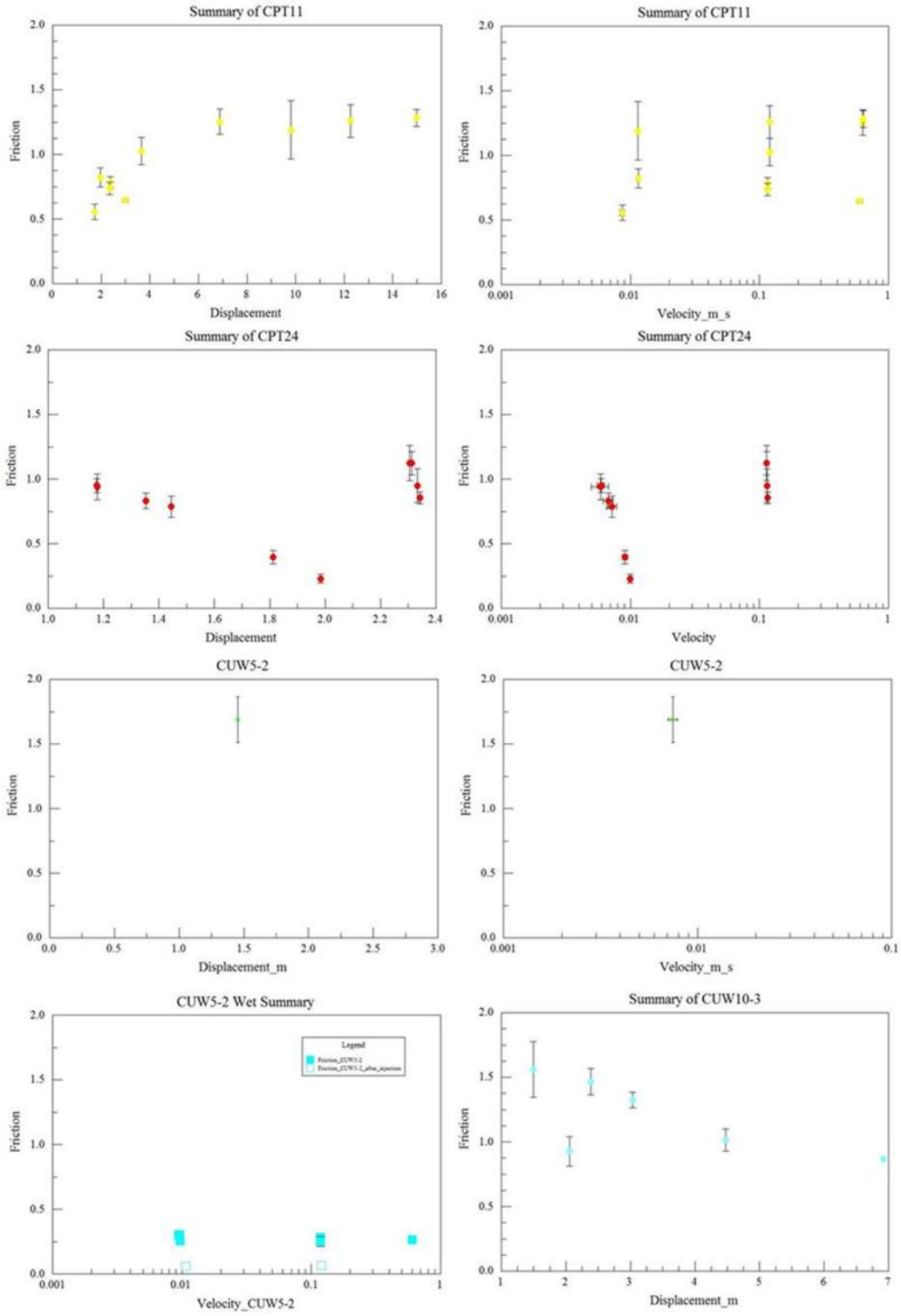

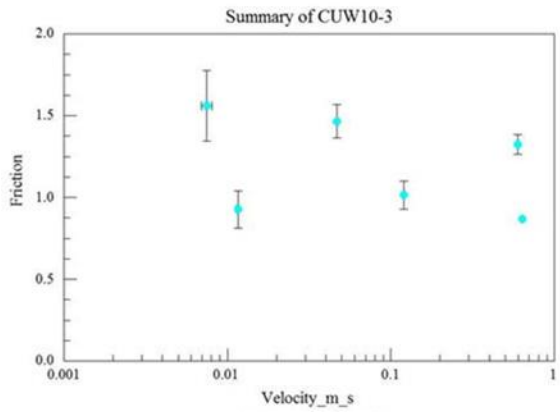
Summary of CUW10-3
Friction
Velocity_m_s

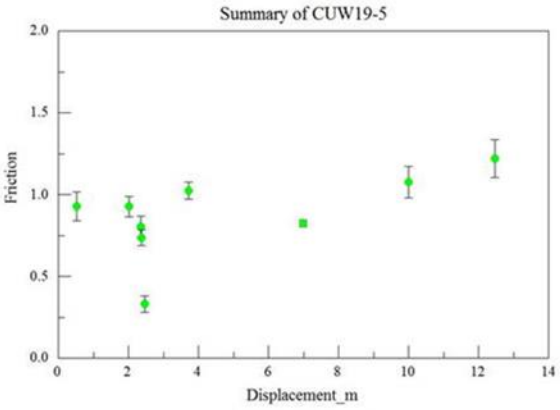
Summary of CUW19-5
Friction
Displacement_m

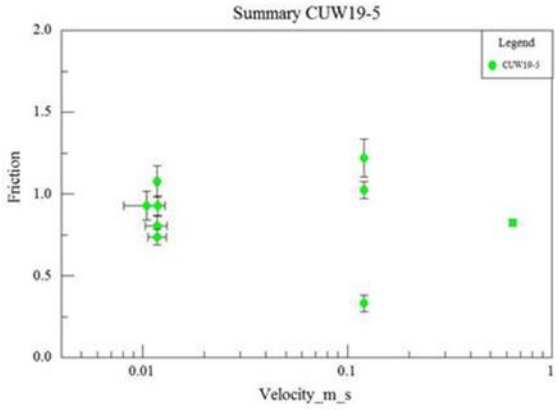
Summary CUW19-5
Legend
CUW19-5
Friction
Velocity_m_s

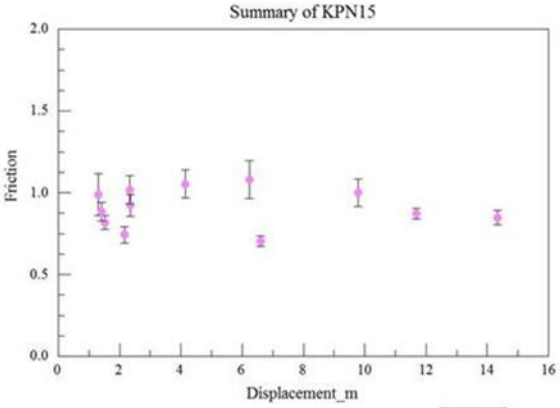
Summary of KPN15
Friction
Displacement_m

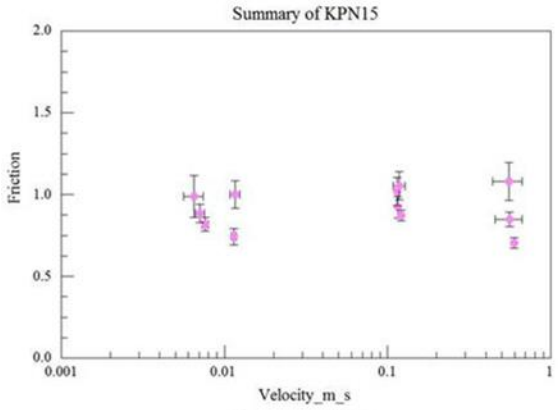
Summary of KPN15
Friction
Velocity_m_s

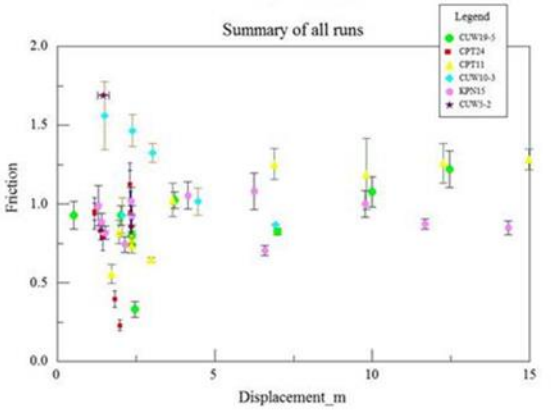
Summary of all runs
Legend
CUW19-5
CPT24
CPT11
CUW10-3
KPN15
CUW3-2
Friction
Displacement_m

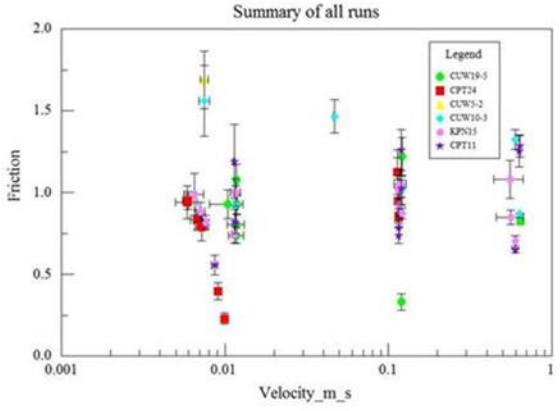
Summary of all runs
Legend
CUW19-5
CPT24
CUW3-2
CUW10-3
KPN15
CPT11
Friction
Velocity_m_s

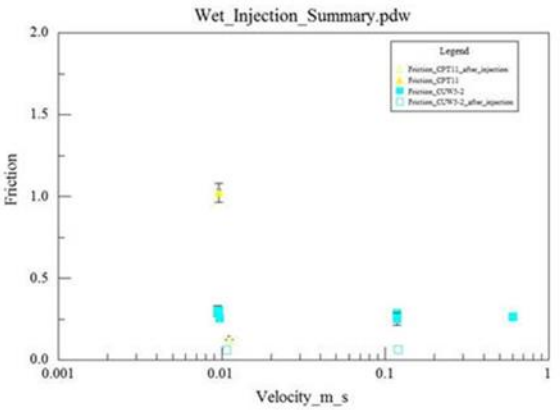
Wet_Injection_Summary.pdw
Legend
Friction
Velocity_m_s

Appendix C: Experimental results descriptions

Reservoir Rocks

Experimental conditions are listed in Tables 3 and 4. This section only summarizes the general results and synthesis is presented later.

Seven experiments were performed on sample RS-QZ22-CC53-CL25 (runs 3270, 3270A, 3271, 3272, 3273, 3274, 3552). The five experiments with no leaks resulted in an average friction coefficient ranging from 0.74 to 0.93 with slight slip strengthening, and a temperature increase of 10-20°C.

Thirteen experiments were run on sample RS-QZ07-CC90-CL03 (runs 3275, 3276, 3277, 3278, 3279, 3280, 3281, 3282, 3283, 3284, 3285, 3286, and 3505). The ten experiments with no leaks resulted in an average friction coefficient ranging from 0.23 to 1.12 with no clear trend of strengthening or weakening, and a temperature increase of 0-10°C.

Twelve experiments were run on sample RS-QZ40-CC00-CL59 (runs 3287, 3288, 3289, 3290, 3291, 3292, 3316, 3317, 3318, 3320, 3321, and 3322). The six experiments with no leak resulted in an average friction coefficient ranging from 0.56 to 1.28 in room-dry conditions and 0.10 to 0.56 in water-saturated conditions with injection. A slight temperature increase of 2-3°C was observed.

Eight experiments were performed on sample RS-QZ32-CC62-CL06 (3296, 3297, 3298, 3299, 3300, 3301, 3302, and 3550). The four experiments with no leak resulted in an average friction coefficient ranging from 0.67 to 1.01 with complex trends in the dynamic friction values. These experiments did not display a trend of strengthening or weakening, and show only slight temperature rise.

Eight experiments were run on sample RS-QZ32-CC17-CL51 (3303, 3304, 3305, 3306, 3307, 3308, 3470, and 3475). The six experiments with no leaks resulted in an average friction coefficient ranging from 0.71 to 1.02 with complex trends in the dynamic friction values. There were no observed trends of strengthening or weakening, but a large temperature rise of 100°C.

One experiment was run on sample RS-QZ09-CC83-CL08 (3314), which resulted in an average friction coefficient of 0.99 and showed slip strengthening of the material. A small temperature rise was observed of a few degrees.

Sedimentary mixtures of quartz-calcite-clay (QCC)

QCC composition 30-70-00, was used for three separate experiments (3540, 3547, 3548). The velocity ranged from 0.001 to 0.32 m/s, cumulative displacements of 10 m, and an average friction coefficient ranging 0.4 to 1 with slip-strengthening.

QCC with 30-00-70, was run in two experiments (3541 and 3543). Velocity ranged from 0.002 m/s to 0.2 m/s, cumulative displacements of 0.7 m, and an average friction coefficient ranging 0.1 to 0.5 with very gentle displacement –strengthening.

QCC with 30-35-35, was used in two experiments (3544 and 3545). The velocity ranged from 0.0001to 0.2 m/s, cumulative displacement of 6.5 m, and the dynamic friction coefficient varying between 0.4 and 0.8 with velocity strengthening behavior observed.

QCC with 30-20-50, was used in five separate experiments (3546, 3551, 3552, 3553, 3554). The velocity ranged from 0.005 m/s to 0.003 m/s with displacement of 10.5 m. A trend of slip-strengthening from initial friction coefficient of 0.3 strengthening to 0.96.

QCC with 30-50-20, quartz-calcite-clay, was used in two experiments (3549 and 3550). Both resulted in an average frictional coefficient of 0.52 with cumulative slip distances of 10.4 m and 8.2m.

QCC with 50-00-50, quartz-calcite-clay, was used in four separate experiments (3555, 3556, 3557, 3558). The velocity ranged from 0.001 to 0.3 m/s and displacement up to 10 m. Velocity and slip –strengthening are observed with dynamic friction values ranging from 0.3 to 0.7.

QCC with 50-50-00, quartz-calcite-clay, was used for two separate experiments (3559 and 3560). Velocity ranged from 0.0004 to 0.3 m/s with cumulative slip distances of 9.6 m. The material remained very stable showing no reaction to velocity steps or displacements and remained at a constant friction coefficient of ~0.7. Run 3560 was a single velocity experiment with a higher velocity than the previous experiment (0.3 m/s) which resulted in a slip -strengthening up to a friction coefficient of 0.92.

QCC with 50-35-15, quartz-calcite-clay, was used for two separate experiments (3561 and 3562). Velocity ranged from 0.001 to 1 m/s with cumulative slip distances of 18 m. Complex trends of velocity strengthening with an average friction coefficient of 0.6 to 1.0.

Appendix D: Mechanical results – Alpine fault

Below are figures of Friction coefficient vs Cumulative slip-distance of all completed experiments. The figures display dynamic friction, stepped-velocity and CO2 emission as a function of slip-distance (m) when recorded.

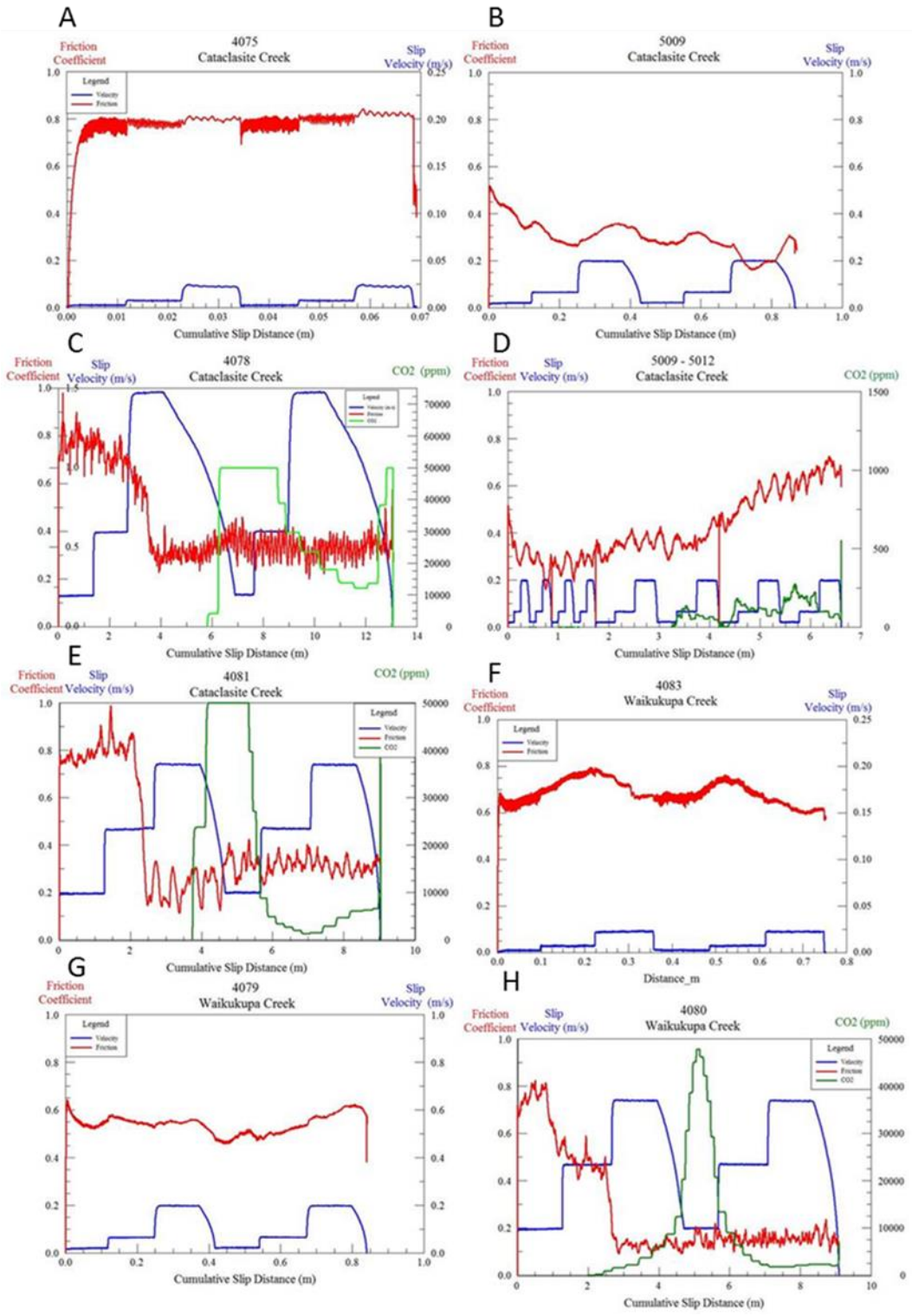
A
4075
Cataclasite Creek
Friction Coefficient
Slip Velocity (m/s)
Cumulative Slip Distance (m)
B
5009
Cataclasite Creek
Friction Coefficient
Slip Velocity (m/s)
Cumulative Slip Distance (m)
C
4078
Cataclasite Creek
Friction Coefficient
Slip Velocity (m/s)
CO2 (ppm)
Cumulative Slip Distance (m)
D
5009 - 5012
Cataclasite Creek
Friction Coefficient
Slip Velocity (m/s)
CO2 (ppm)
Cumulative Slip Distance (m)
E
4081
Cataclasite Creek
Friction Coefficient
Slip Velocity (m/s)
CO2 (ppm)
Cumulative Slip Distance (m)
F
4083
Waikukupa Creek
Friction Coefficient
Slip Velocity (m/s)
Distance_m
G
4079
Waikukupa Creek
Friction Coefficient
Slip Velocity (m/s)
Cumulative Slip Distance (m)
H
4080
Waikukupa Creek
Friction Coefficient
Slip Velocity (m/s)
CO2 (ppm)
Cumulative Slip Distance (m)

I

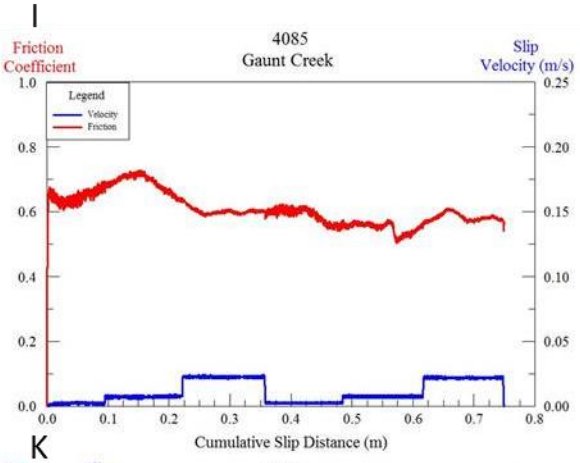
4085
Gaunt Creek
Friction Coefficient
Slip Velocity (m/s)
Legend
Velocity
Friction
Cumulative Slip Distance (m)

J

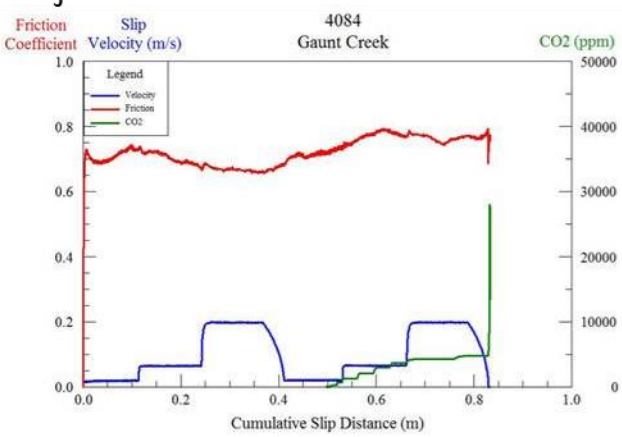
4084
Gaunt Creek
Friction Coefficient
Slip Velocity (m/s)
CO2 (ppm)
Legend
Velocity
Friction
CO2
Cumulative Slip Distance (m)

K

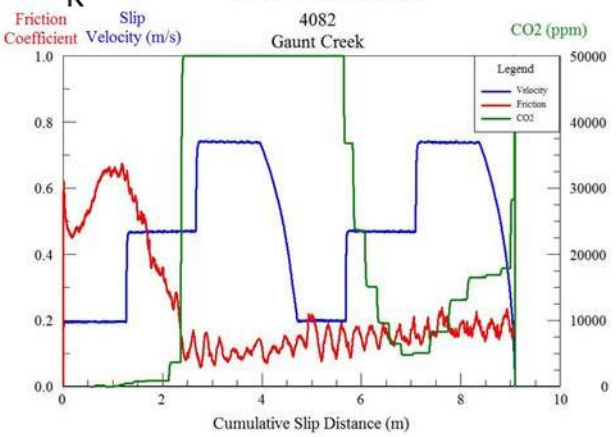
4082
Gaunt Creek
Friction Coefficient
Slip Velocity (m/s)
CO2 (ppm)
Legend
Velocity
Friction
CO2
Cumulative Slip Distance (m)

Appendix D: CO_2 and Temperature vs Time

CO2 emission recorded from inside of the CROC indicate extreme heating of the sample during slip. To better delineate the how to two (temperature and CO2) coincide, the figures below are plotted against time.